INVESTIGATION OF LOW-PROFILE VORTEX GENERATORS VIA COMPUTATIONAL METHODS

By

TREVOR WILSON

Bachelor of Science in Mechanical Engineering

Oklahoma State University

Stillwater, Oklahoma

2017

Submitted to the Faculty of the
Graduate College of the
Oklahoma State University
in partial fulfillment of
the requirements for
the Degree of
MASTER OF SCIENCE
July, 2019

INVESTIGATION OF LOW-PROFILE VORTEX GENERATORS VIA COMPUTATIONAL METHODS

Thesis Approved:

Dr. Brian Elbing

Thesis Advisor

Dr. Jamey Jacob

Dr. Aaron Alexander

Dr. Omer San

ACKNOWLEDGMENTS

This work was in part funded by Edge Aerodynamix.

The computing for this project was performed at the OSU High Performance Computing Center at Oklahoma State University supported in part through the National Science Foundation grants OAC1126330 and OAC1531128.

First, I would like to thank my parents, Rick and René, for their unwavering love and support through my life and academic journey. Also, I would like to thank my wonderful girlfriend Annagrace, for loving and believing in me. Next, I would like to thank my friends Real and Nick, for their help and friendship, which made this all possible. Finally, I would like thank my committee, whose guidance and support has been crucial throughout this process.

Name: TREVOR WILSON

Date of Degree: JULY, 2019

Title of Study: INVESTIGATION OF LOW-PROFILE VORTEX GENERATORS VIA COMPUTATIONAL METHODS

Major Field: MECHANICAL AND AEROSPACE ENGINEERING

Abstract: A unique low-profile vortex generator, termed the Conformal Vortex Generator (CVG), has recently been discovered to provide fuel saving of greater than 1% on commercial aircraft. The CVG is an adhesive backed film that creates a spanwise varying aft facing step. While the CVG has been shown to provide fuel savings, the driving fluid mechanism behind the CVG is still unknown. The current work aims to understand and validate the behavior of the CVG at subsonic conditions as well as investigate the behavior of both the CVG and traditional aft facing step at supersonic conditions. The subsonic simulations used a model based on water tunnel and flight test experiments. The goal of these simulations was validation and to provide data not available through experimentation. This study concluded that the simulations could successfully model the flow over a CVG by showing strong qualitative and quantitative similarities between computational and experimental data. It was also shown that the CVGs imparted strong spanwise variations in the boundary layer and wall shear stress that had both a Re_H and CVG length (L) to width (W) ratio dependence. The second set of simulations were based on flight scale conditions (the same as seen in the CVG real world application) and investigated the local flow physics of the CVG. These simulations were performed with a local freestream Mach number of 1.3 and an altitude of 10,000 m. It was shown that at these conditions, the CVG behavior still exhibits L/W ratio dependence and spanwise variation in the boundary layer thickness and wall shear. However, the results varied from the subsonic scaling. The CVGs also impart spanwise varying vorticity into the flow that is not consistent with a traditional step. Lastly, it was concluded that the addition of a downstream ramp past an aft facing step can mitigate the supersonic expansion fan that occurs over a step in supersonic flow.

TABLE OF CONTENTS

LIST OF TABLES

LIST OF FIGURES

Figure Page

Figure Page

NOMENCLATURE

BFS = Backward Facing Step

c = chord

CVG = Conformal Vortex Generator

C_f = coefficient of friction

C_l = coefficient of lift

C_n = coefficient of normal force

C_p = coefficient of pressure

g = gravitational force

H = CVG height or shape factor

p = pressure

Re = Reynolds number

Re_c = Reynolds number based on chord length

Re_H = Reynolds number based on CVG height

Re_x = Reynolds number based on downstream distance

t = time

u = streamwise velocity (x-direction)

U = average inlet velocity

U_∞ = free-stream velocity

v = vertical velocity (y-direction)

w = spanwise velocity (z-direction)

W = CVG width

x = downstream distance

α = angle of attack

δ = boundary layer thickness

δ^* = boundary displacement thickness

δ_{99} = boundary layer thickness at 99% U_∞

μ = dynamic viscosity

ν = kinematic viscosity

ρ = density

θ = boundary momentum thickness

CHAPTER I

INTRODUCTION

1.1. Motivation

Transportation industries all share a common priority; increasing fuel efficiency. One way this can be achieved is through increasing the aerodynamic performance of their respective means of transportation (e.g. drag reduction). A common way to improve this performance on airliners is through flow control. Flow control is achievable through active and passive methods. Active methods are typically able to achieve higher amounts of drag reduction, but at the cost of design complexity, maintenance, and operational energy. Thus, passive methods are more frequently used, with one of the most common and impactful being the vortex generator (VG). They can be implemented in a variety of applications including use on aircrafts, automobiles, and wind turbines. VGs are commonly used due to their ability to increase lift, reduce drag (in certain applications), and stabilize supersonic shock waves [1]. These effects occur due to the VG's ability to induce vortex structures into a flow regime that energize the boundary layer [2]. Despite these benefits, the traditional VG has one major flaw, increased parasitic drag. This parasitic drag is introduced due to the size of the VG. Traditional VGs protrude into the flow on the order of the boundary layer thickness. Low-profile vortex generators (LPVGs) have been developed to try and mitigate this issue [1]. However, since most LPVGs have a similar geometry to the traditional

VG with simply a smaller height, they tend to have a weaker impact on the flow. In an attempt to remedy this issue, a new type of low-profile vortex generator was created and termed the Conformal Vortex Generator (CVG). Flight testing has provided evidence that the CVG provides a fuel saving of greater than 1% when applied on a Boeing 737 [3], but the mechanism is unknown. This prevents development of an ideal geometry. Further background information regarding the CVG is provided in section 2.2. The current work focuses on the investigation of the local impact of the CVG by utilizing computational simulations.

1.2. Goals and Objectives

The goal of this study was to investigate the flow field induced by the CVGs via high fidelity computational simulations on a flat plate and an airfoil model. The primary objectives were to validate simulations with experimental data and use these validated simulations to identify the dominant flow features produced by the CVG, which would provide insight into the fluid mechanism responsible for drag reduction observed on Boeing 737 aircraft equipped with CVGs. For the flat plate water tunnel study, the following aims were carried out:

- Validate the clean flat plate boundary layer with experimental data. Compare simulation results with the Blasius boundary layer solution and experimentally obtained data.
- Validate flat plate with CVGs by comparing the velocity profiles at different locations downstream of the CVG with experimental data.
- Utilize these validated simulations to study the impact of the CVG as well as compare with flight testing data.

For the flight scale study, the following tasks were carried out:

- Study the effects of the CVG at flight conditions that match the Boeing 737.
- Validate simulations of a 2D RAE 2822 airfoil with experimental data for the purpose of investigating the effect of an aft facing step and a downstream ramp.
- Study the local effects of a aft facing step in a supersonic flow with a downstream ramp.

CHAPTER II

BACKGROUND AND THEORY

2.1. Vortex Generators

Vortex generators (VGs) are a common passive flow control device used in a wide variety of industries, including transonic aircraft, small ultralight aircraft, and even automobiles [4–6]. While all of these industries utilize VGs, the desired impact of the VGs change. Aircraft that operate in the transonic and supersonic regimes see benefits from VGs through mitigation of the interaction between shocks and the boundary layer [7], while small ultralight aircraft utilize VGs to reduce stall speed which provides an enhancement in aileron maneuverability [8]. For ground based vehicles, VGs have been shown to decrease drag as well as increase downward force [9, 10]. While the application of the VG varies, the enhancements are all achieved through the addition of momentum into the boundary layer of a flow. An example of vortex generators applied to a commercial airliner can be seen in Fig. 1.

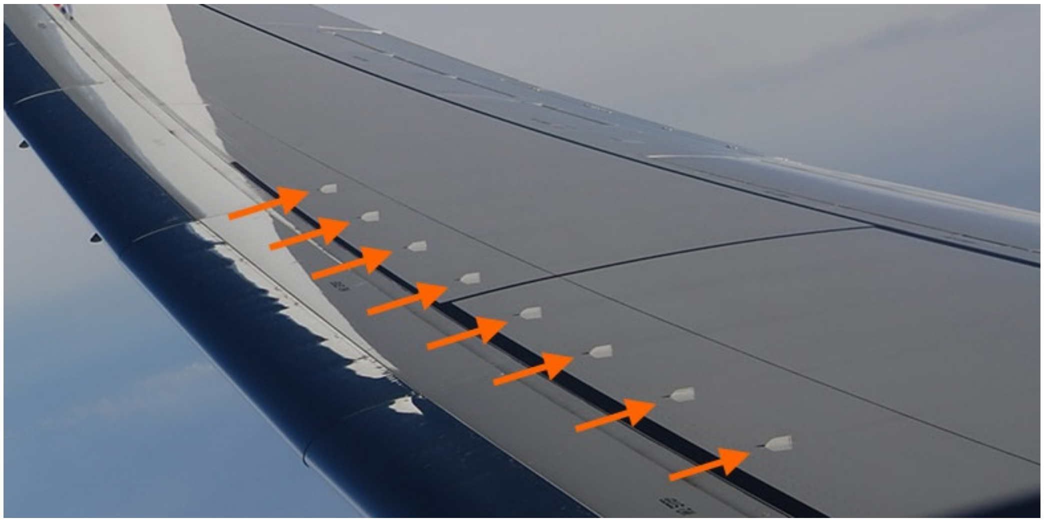

Figure 1: An example of a vortex generators used on a Boeing 737-800 wing [11]

2.2. Conformal Vortex Generators

2.2.1. Background

This study focuses on a specific vortex generator, termed the Conformal Vortex Generator (CVG) (seen in Fig. 2). The CVG is a thin adhesive backed film with triangular shaped serrated edges. The CVG was originally developed by Edge Aerodynamix (EA) for the purpose of mitigating losses associated with the application of leading edge protective tapes for rotor craft blades [12]. Leading edge tapes are installed on rotor crafts to prevent damage and erosion of the blades, but this protection comes at the cost of increased profile drag [13]. The EA CVG was found to not only protect the blades, but increase the fuel efficiency of the helicopter. Following this discovery, the CVG was tested on a range of aircraft, with a primary focus on the Boeing 737-500. The CVG installed on the Boeing 737 is located just downstream of the slat step (approximately 10% chord) with a tape thickness of 0.367 mm. This location can be seen in detail in Fig. 3. While it was concluded that the CVG could increase fuel efficiency for both of these applications, little was known about the driving mechanism behind this result.

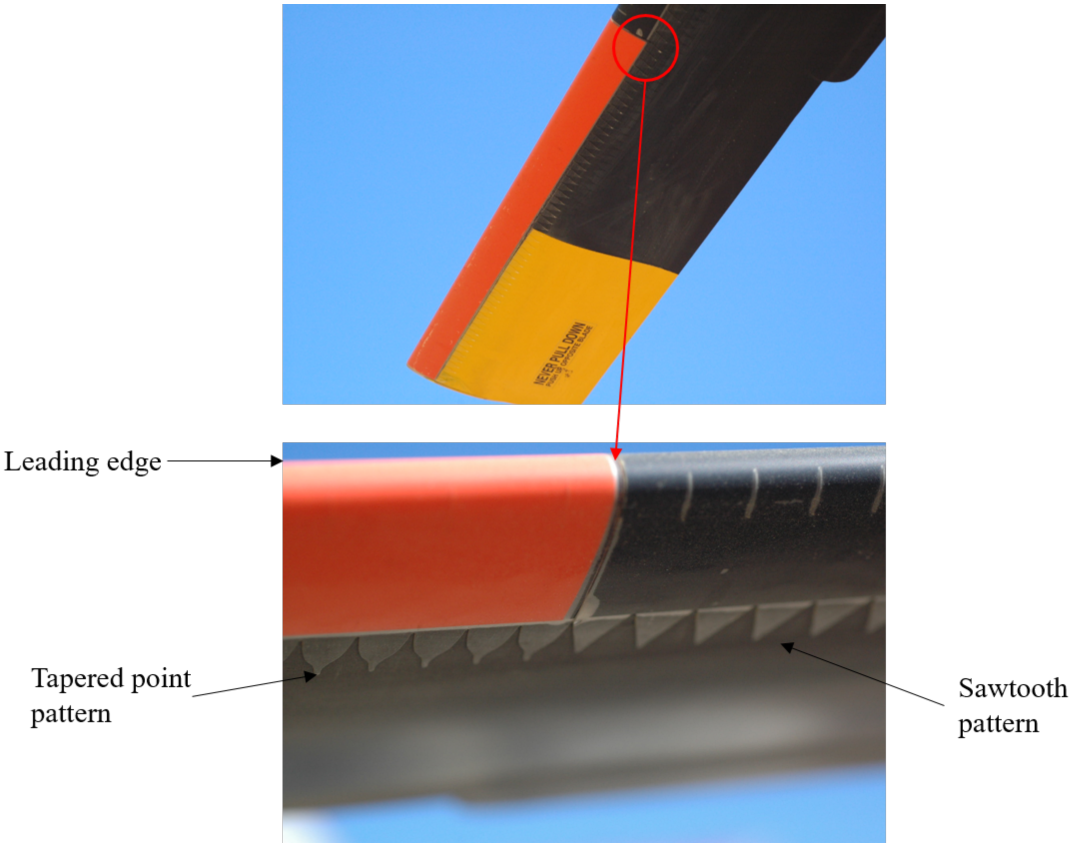

Figure 2: Two diffrent configurations of CVGs applied to a helicopter blade. Top image shows the overall application while the bottom shows the two different CVG types [12].

2.2.2. Wind Turbines

A study was conducted by the National Renewable Energy Laboratory (NREL) to investigate the use of CVGs on wind turbines [14]. Tapes, similar to the CVG, are applied to the leading edge of wind turbine blades for several purposes, including improving the power capture of the turbine and/or protecting the blade to extend its lifetime. The purpose of this study was to investigate if the CVG performed differently than commercially available leading edge tapes. An example of how the CVGs were applied to the blades can be seen in Fig. 4. The turbines tested were 2-bladed Westinghouse WWG-0600 turbines with a total rotor diameter of 44 m. The parameter that was used for comparison between the tapes was the power output of the turbine. This study showed a KWH production increase of 6% and

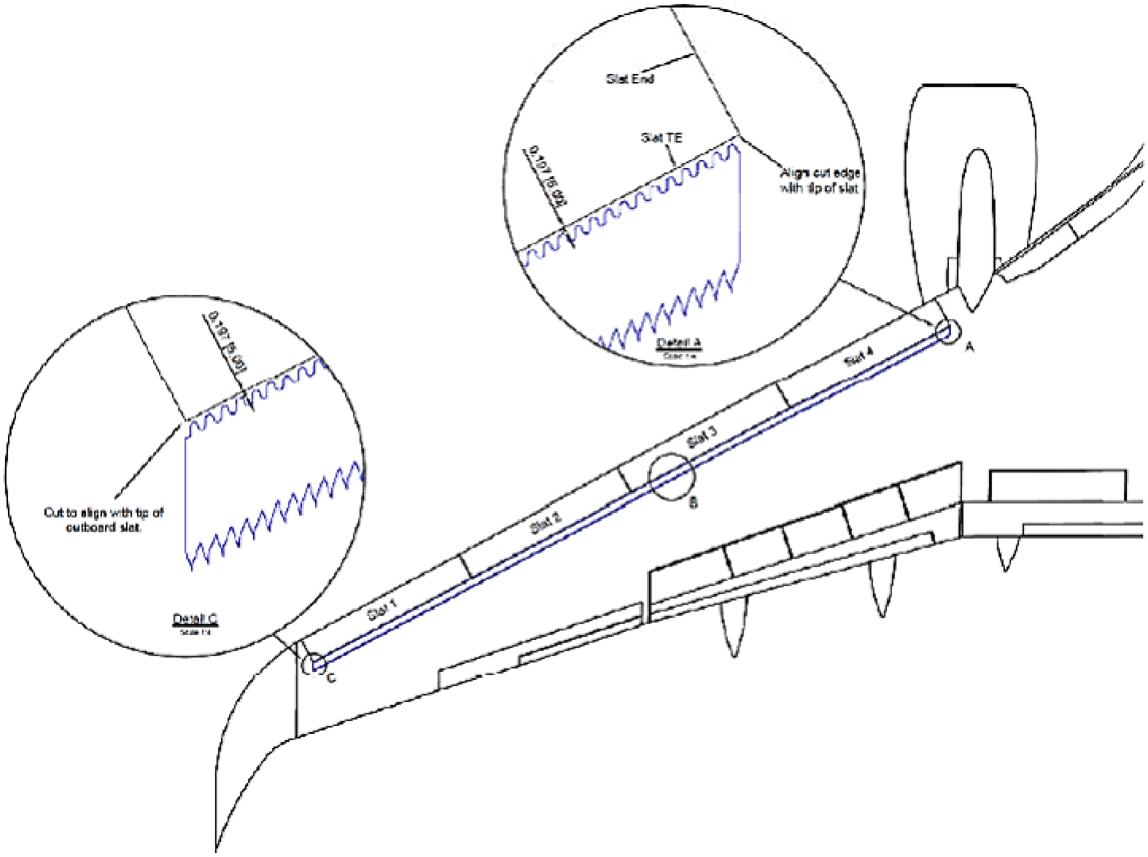

Figure 3: Schematic of the CVG tape applied to the Boeing 737 aircraft. The blue outline demonstrates the location of CVGs [12].

7.4% for the CVG at wind speeds of 7 m/s and 11 m/s, respectively. The sole purpose of this study was to analyze the change in turbine efficiency. Therefore, no additional information was provided regarding the fluid mechanism behind this result.

2.3. Governing Equations

The governing equations that are the basis of the simulations used in the the current study are shown in equations 1 and 2

The continuity equation is given as:

$$\frac{1}{\rho}\frac{D}{Dt}\rho + \nabla \cdot \vec{u} = 0. \tag{1}$$

Figure 4: CVG applied to the NREL Wind Turbine [14].

The Navier-Stokes equations are given as:

$$\rho \frac{Du_j}{Dt} = -\frac{\partial p}{\partial x_j} + \rho g_j + \mu \frac{\partial^2 u_j}{\partial {x_i}^2} + (\mu_v + \frac{1}{3}\mu)\frac{\partial}{\partial x_j}\frac{\partial u_m}{\partial x_m}. \tag{2}$$

2.4. Boundary Layer

2.4.1. Laminar Boundary Layer

Laminar boundary layer theory is well defined, specifically for a flat plate with zero pressure gradient. This zero pressure gradient flat plate is the type of boundary layer investigated in Chapter IV. An exact solution exists for this condition, known as the Blasius solution [15]. The Blasius solution provides equations 3, 4, and 5. Displacement thickness, δ^*, is the distance the wall would be outwardly displaced to maintain the mass flux in a hypothetical flow with no friction. Momentum thickness, θ, is the amount of momentum that is lost in a flow due to the boundary layer. Finally, the shape factor is a ratio of the two and is used to determine the nature of the flow (laminar vs turbulent) [15]. The 99% boundary layer thickness (δ_{99}) for the Blasius solution is:

$$\delta_{99} = \frac{4.92x}{{Re_x}^{1/2}}. \tag{3}$$

The displacement thickness is given as:

$$\delta^* = 1.72\sqrt{\frac{\nu x}{U}}. \tag{4}$$

The momentum thickness is given as:

$$\theta = 0.644\sqrt{\frac{\nu x}{U}}. \tag{5}$$

The shape factor is given as:

$$H = \frac{\delta^*}{\theta} = 2.67. \tag{6}$$

2.4.2. Transition

When a boundary layer begins to transition from laminar to turbulent, the Blasius solution no longer holds. Transition can be caused in a multitude of ways, several of which include the laminar boundary layer becoming unstable or forcing transition through a forced mechanism. The location in which this transition occurs is very important. For an airfoil, it is typically better if the flow transitions at the furthest downstream location possible, as this results in the least amount of drag. This point of transition can be delayed utilizing VGs similar to those discussed in vortex generator section of this chapter [16]. However, due to laminar flows being more likely to separate, it can also be advantageous to force transition at a specific location on an airfoil with a boundary layer trip. Therefore, controlling transition is a vital aspect of flow control. Fig. 5 shows a schematic of flow over a flat plate that demonstrates the step involved in transition.

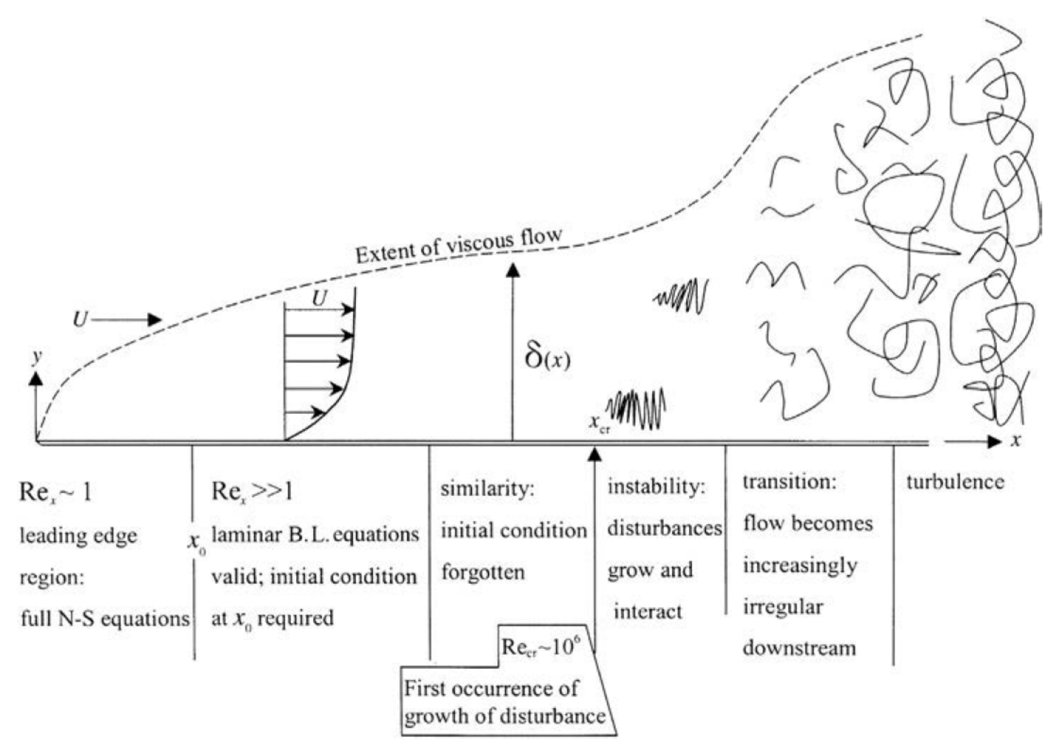

Figure 5: Schematic of flow over over a flat plate. The location of transition can be seen near the end of the flow, right before the onset of turbulence [15]

2.4.3. *Turbulent Boundary Layer*

A flow transitions from laminar to turbulent if there is a disturbance in the flow or the Reynolds number is sufficiently high (the exact Reynolds number where this happens is highly flow dependent). In most applications on aircraft wings, turbulent flow is less desirable than laminar. This is due to the turbulent boundary layer being thicker and generating more skin friction drag. However, as mentioned in the transition section, a turbulent boundary layer is less likely to separate and can be desirable in cases where the goal is to prevent separation.

One of the most important concepts when trying to understand a turbulent boundary layer is the law of the wall. The law of the wall states that in a turbulent boundary layer, the flow at a certain height is proportional to the distance from the wall [17]. The law of the wall can be seen in Fig. 6. The near wall region is termed the viscous sublayer (or laminar sublayer). In this region, the viscous forces dominate the flow. This region is defined by,

$$u^+ = y^+, \tag{7}$$

and holds true for $y^+ < 5$. Here the viscous wall unit (y^+) is,

$$y^+ = \frac{y u_\tau}{\nu}, \tag{8}$$

the dimensionless velocity (u^+) is,

$$u^+ = \frac{u}{u_\tau}, \tag{9}$$

and the friction velocity (u_τ) is,

$$u_\tau = \sqrt{\frac{\tau_w}{\rho}}. \tag{10}$$

This regions length scale is defined by the viscous sublayer length scale (ℓ_ν), which is defined as,

$$\ell_\nu = \frac{\nu}{u_\tau}. \tag{11}$$

The next region is the log-law region ($y^+ > 30$) where the law of the wall states that the velocity is proportional to the logarithm of the wall distance. The equation for this regime is,

$$u^{+} = \frac{1}{\kappa} \ln y^{+} + C, \tag{12}$$

where the most common values of κ and C used are 0.41 and 5 (for a smooth wall) respectively. The region between these two ($5 < y^{+} < 30$) is the buffer layer where neither Eqs. 7 or 12 hold. More details and the derivation of these parameters can be found in Kundu's "Fluid mechanics" [15].

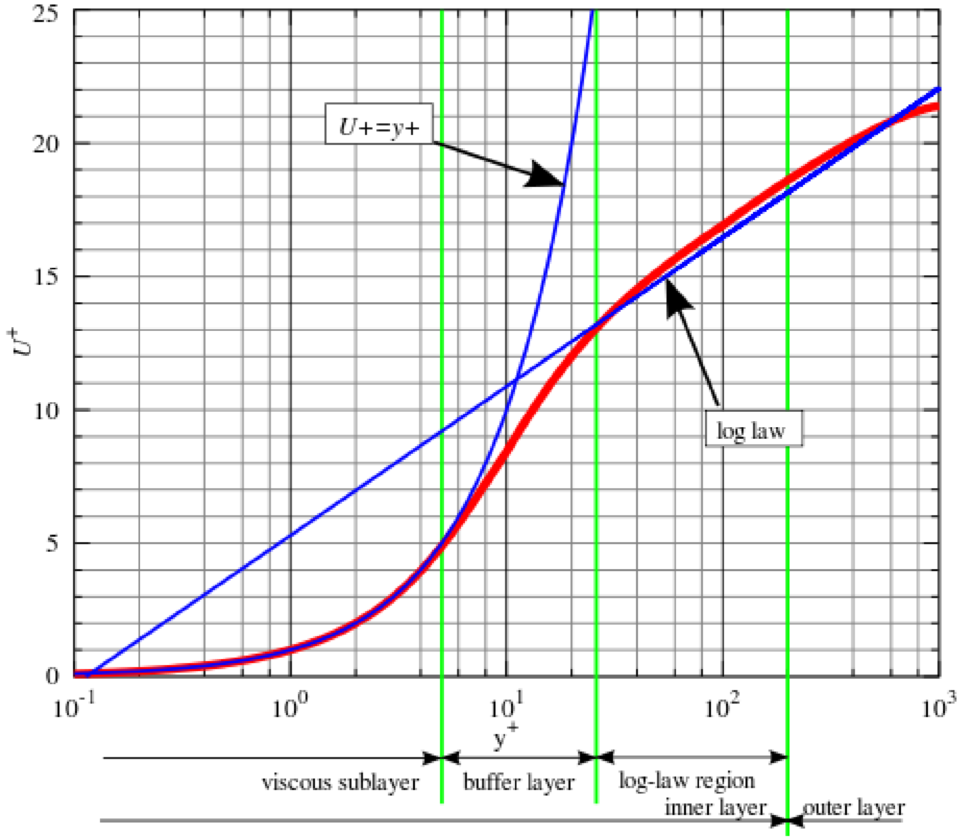

Figure 6: Law of the wall derived by Theodore von Karman [17].

2.5. Computational Models

2.5.1. Computational Fluid Dynamics (CFD)

Computational fluid dynamics (CFD) is the method of utilizing computers to solve the governing partial differential equations that describe fluid flow and their related phenomena. These governing equations (Eqs. 1 and 2) cannot be solved analytically except in specific cases. Therefore, a discretization method is used to obtain an approximate solution to these equations by transforming these partial differential equations into systems of algebraic equations. These algebraic equations are applied to a discrete domain and utilized to solve for flow properties at locations in space and time. While this method is extremely useful in solving for flow parameters, the accuracy of CFD solutions depend heavily on the quality of discretization utilized [18].

2.5.2. Direct Numerical Simulation (DNS) and Reynolds-Averaged Navier-Stokes (RANS)

The most accurate approach to modeling a turbulent flow is through the utilization of Direct Numerical Simulation (DNS) where the Navier-Stokes equations are solved without approximation. Due to the wide range of scales in a turbulent flow, DNS carries an extreme computational cost. However, in most cases, the mean characteristics of a flow is the most insightful. Therefore, instead of solving the Navier-Stokes equations (Eq. 2) instantaneously, one can utilize the Reynolds-averaged Navier-Stokes equations (RANS). The RANS equations are,

$$\frac{\partial(\rho\overline{u_i})}{\partial t} + \frac{\partial}{\partial x_j}\left(\rho\overline{u_i}\overline{u_j} + \rho\overline{u_i' u_j'}\right) = -\frac{\partial\overline{p}}{\partial x_i} + \rho\overline{g_i} + \frac{\partial}{\partial x_j}\left(\mu\left(\frac{\partial\overline{u_j}}{\partial x_j} + \frac{\partial\overline{u_j}}{\partial x_i}\right)\right). \tag{13}$$

These equations are derived utilizing the Reynolds decomposition, which states a scalar quantity can be represented as the sum of the mean value and the fluctuations about the mean as:

$$\Phi = \overline{\Phi} + \Phi'(t). \tag{14}$$

However, this derivation leads to a set of equations that is not closed, meaning that there are more unknowns than equations. To close the RANS equations, turbulence models (i.e. k-ω, k-ϵ, etc.) are utilized to approximate the parameters needed. Due to the utilization of a commercial CFD package in this study, the derivation of these models will not be shown but can be found in Ferziger's book, "Computational Methods for Fluid Dynamics" [18].

2.5.3. Large Eddy Simulation (LES) and Detached Eddy Simulation (DES)

Large Eddy Simulation is a method of solving the Navier-Stokes equations that is a middle ground between DNS and RANS. LES utilizes filtering to lessen the computational cost at the expensive of not resolving the smallest scales of the flow. Instead, LES focuses on resolving the large, energy dominant features of a flow that provide the most transport of properties. It then utilizes low-pass filters to obtain an equation for the large scale flow features. The LES equations are,

$$\frac{\partial \bar{u}_i}{\partial t} + \bar{u_j}\frac{\partial \bar{u}_i}{\partial x_j} = -\frac{1}{\rho}\frac{\partial \bar{p}}{\partial x_i} + \nu\frac{\partial^2 \bar{u}_i}{\partial x_j \partial x_j} - \frac{\partial \tau_{ij}}{\partial x_j}. \tag{15}$$

Here τ_{ij} is,

$$\tau_{ij} = \overline{u_i u_j} - \bar{u}_i \bar{u}_j, \tag{16}$$

and is called the subgrid-scale (SGS) Reynolds stress. This Reynolds stress contains the local averages of the small scale flow features and is approximated utilizing SGS modeling. More information on these SGS models can be found in Ferziger's book, "Computational Methods for Fluid Dynamics" [18]. A method that utilizes the benefits of both LES and RANS is Detached Eddy Simulation (DES). DES utilizes a RANS solution in regions where the turbulent length scale is smaller than the grid sizing and LES in regions where the grid sizing is smaller than the length scale. DES is utilized in situations where the higher computational cost of LES is too demanding [19].

CHAPTER III

COMPUTATIONAL METHODS

3.1. OSU HPCC

The Oklahoma State University High-Performance Computing Center (HPCC) has two computational clusters, "Cowboy" and "Pete". These clusters were vital to this investigation as computational simulations were run on 10 to 50 nodes (or 120-600 processors), and allowed for the use of extremely fine meshes to be utilized in the CFD simulations. The typical run time for a simulation was 10 days, resulting in utilization of 30,000-150,000 core hours per simulation.

Cowboy was acquired from Advanced Clustering Technologies and was funded by the National Science Foundation (NSF) grant OCI-1126330. Cowboy consists of 252 standard compute nodes consisting of dual Xeon E5-2650 hex core CPUs (with clock speed of 2.0 GHz) as well as 32 GB of RAM (with a speed of 1333 MHz). The cluster also contains two fat nodes, each having 256 GB of RAM and also a NVIDIA Tesla C2075 graphics card. This totals to 3,048 cores, 8,576 GB of RAM, an aggregated peak speed of 48.8 TFLOPs, and a total shared disk space of 92 TB.

Pete was also acquired from Advanced Clustering Technologies and was funded by the MRI Award 1531128. This cluster consists of 164 standard compute nodes, each with two Intel 6130 CPUs and 96 GB of RAM. Pete has two large memory nodes that consist of the same CPUs but instead have 768 GB of RAM. Pete utilizes a 100 GB/s Intel Omni-Path low-latency interconnect and a 360 TB high-speed parallel file system.

3.2. Star-CCM+

The CFD software utilized in this study was Star-CCM+ developed by Siemens, a commercial CFD package designed for use in engineering applications. The specific capabilities discussed below outline why Star-CCM+ was chosen and was instrumental in executing this study. Star-CCM+ contains a built in 3D CAD, which was utilized to construct most of the simulation geometries. However, since the CAD package only provides basics tools, parasolid files were imported when the geometry for simulations were too complex. Star-CCM+ also provides built in automated meshing capabilities including the production of tetrahedral, trimmer hexahedral, and polyhedral unstructured meshes. The previously mentioned algorithms also have the capability of utilizing prism layers, which help resolve the boundary layer of a flow in the near wall region. Additionally, Star-CCM+ has the capability to run a large range of physics and flow specific models. These models include RANS, DES, LES, and qDNS, with multiple sub-models for each. More information regarding these models can be found in Chapter II.

3.3. Solver

Quasi-Direct Numerical Simulation (qDNS), also known as Wall-resolved Large Eddy Simulation (LES) was used for all simulations in this study due to the size of the flow features being analyzed. It was necessary to use a solver that would resolve and not model the near wall flow characteristics. qDNS is based on an LES model but can turn off the sub-grid scale model in the attempt to properly resolve the near wall features. This is accomplished by incorporating an extremely fine mesh in the near wall region. The governing fluid partial differential equations were solved with a finite volume method utilizing an implicit second order temporal discretization and a bounded-central discretization for the convection terms of the equations. Two solution procedures were used to solve the governing equations. A segregated method was used for all water based simulations while a coupled method was used for air based simulations. The segregated method solves the equation for a single variable for all cells and then moves on to the next variable, while the coupled method solves for all variables in a given cell and then repeats for all cells in the simulation. A segregated method is best for standard incompressible flows while coupled is best when dealing with supersonic flows involving shocks and expansion fans.

3.4. Mesh

All of the meshes for the simulations were constructed utilizing the built in automated mesher of Star-CCM+. Since qDNS was the selected solver for this investigation, a high density mesh was required. To try and capture the near wall aspects of the boundary layer, the first cell mesh size needed to be on the order of the viscous sublayer length scale (ℓ_v) (Eq. 11) in the vertical direction. This requirement is caused by the use of qDNS. Since the subgrid model is disabled, which would typically model the flow in the buffer and viscous sublayers, there needs to be adequate resolution to resolve the full boundary layer (see section 2.4.3). This value is on the order of 10^{-6} m for the air based simulations and 10^{-5} m for the water based simulations. Prism layers were then used along the bottom wall of the simulations to achieve this high density mesh in the near wall region. Twenty layers were used with their vertical spacing growing from <1 ℓ_v to 10 ℓ_v, at the wall and top of the boundary layer respectively. Table based mesh adaptation was also utilized to more accurately capture the supersonic features in the flow. These requirements together meant that the mesh count for the simulations ranged from 20-60 million cells.

3.5. Boundary Conditions

The boundary conditions for the water tunnel based simulations consisted of a velocity inlet, a pressure outlet, periodic side boundaries, walls, and a slip wall. The velocity inlet was set up with the same fluid property conditions as would be seen in the water tunnel. The inlet velocity profile was experimentally found using PIV and then imported into the simulation. The pressure outlet was set up to act as the exit of the water tunnel. A periodic interface was used for the side wall to simulate an infinitely long (in the spanwise direction) flat plate. Normal no-slip walls were used on the bottom surface while a slip wall was used on the upper surface. The slip wall was used to remove the need to adequately resolve the boundary layer that would be forming on the bottom of the water tunnel lid. Due to the height of the simulation, this had negligible impact on the flow characteristics that were being investigated. The boundary conditions for the flight based simulations were identical except for the top wall being replaced by a free stream condition. This approach was chosen as supersonic effects would be greatly altered by the presence of a wall.

CHAPTER IV

SIMULATION I: PIPER CHEROKEE VALIDATION

4.1. Flight Testing

The first experimental tests performed on the CVG analyzed the wall shear downstream of the CVG. These wall shear stress visualization tests, performed by Edge Aerodynamix, applied CVGs on a Piper Cherokee aircraft and then utilized a biphenyl solution to visualize areas of high and low shear [20]. This solution is sprayed on the wing using a technique called "dry-spraying", the process of applying a coating of dry powder to the test surface by having the acetone in the solution evaporate prior to its contact with the test surface. In flight, this powder will be removed by high wall shear leaving white regions (where the powder remains) that have lower shear stress. These low shear regions appear downstream of the valley of the CVG and are termed low shear "diamonds" and are characterized by their length (L_d). The before and after of these tests can be seen in Fig. 7. Additional details of these tests, as well as an analysis of the patterns are provided in [21], [22], and [23].

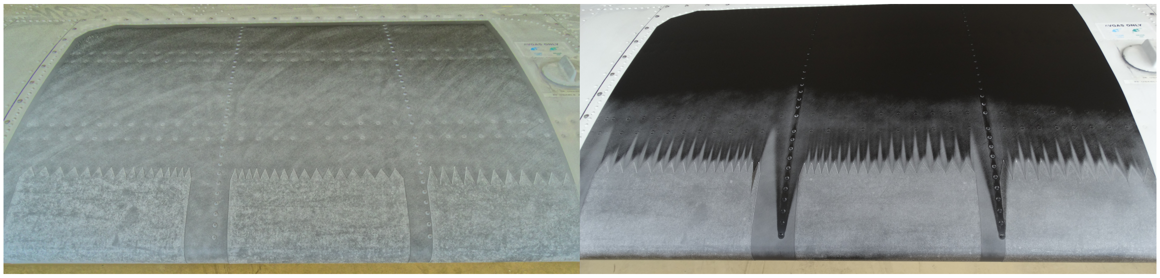

Figure 7: Wall shear visualization on a Piper Cherokee wing utilizing biphenyl solution (a) before, (b) after flight tests.

4.2. Water Tunnel Testing

Flat plate tests were performed in the Experimental Flow Physics Lab at Oklahoma State University to investigate the boundary layer downstream of the CVG. The flat plate and the CVG were scaled to replicate the flow physics seen on the Piper Cherokee wing during flight (details discussed in the Flight Testing section of this chapter) . This scaling was focused on a CVG with laminar boundary layer inlet and vorticity was assumed to be the parameter of interest. The scaling was done assuming that the CVGs impact could be determined based on the following parameters: the inlet boundary layer conditions (thickness (δ), the freestream velocity (U_∞), and the pressure gradient ($\frac{\mathrm{d}p}{\mathrm{d}x}$)), CVG geometry (height, H; width, W; and length L), and the fluid properties (density, ρ; and kinematic viscosity, ν). Utilizing these parameters and dimensional analysis the scaling law,

$$\frac{\omega H}{U_\infty} = \phi\left(\frac{\delta}{H}, \frac{U_\infty H}{\nu}, \frac{\mathrm{d}p}{\mathrm{d}x}\frac{H}{\rho U_\infty^2}, \frac{W}{H}, \frac{L}{H}\right), \tag{17}$$

could be derived. A limitation that was imposed on this scaling was that the CVG's height could only be scaled in integer increments of its original manufactured size (by stacking CVG film layer). The CVG scaling was determined by utilizing Eq. 17, the flight properties of the CVGs, and the height limitation. Despite the height limitation constraining the scaling significantly, several appropriate testing conditions were obtained and can be found in Table 1 (where n is the integer number of CVG heights or film thicknesses).

The flat plate used was 750 mm long by 300 mm wide and had CVGs applied to it

Table 1: Required water tunnel testing conditions based on number of film layers

n	U_∞ (m/s)	δ (mm)	x (mm)
1	4.7	0.7	93
2	2.3	1.4	186
3	1.6	2.1	279
4	1.2	2.8	371
5	0.94	3.5	464
6	0.78	4.2	557

that were scaled best on the methodology explained at the beginning of this section. Particle image velocimetry (PIV) was utilized to extract velocity profiles at a multitude of locations across the plate. It is important to note that the view of the camera was obstructed by the CVG itself and did not allow any data to be taken upstream of the peak. Locations where data could be acquired are shown in Fig. 8. These experimental velocity profiles were used as both inlet conditions and comparison data across different locations on the plate for the computational simulation. Additional details of the experiments, including scaling, results, and analysis, can be found in [23], [24], and [25].

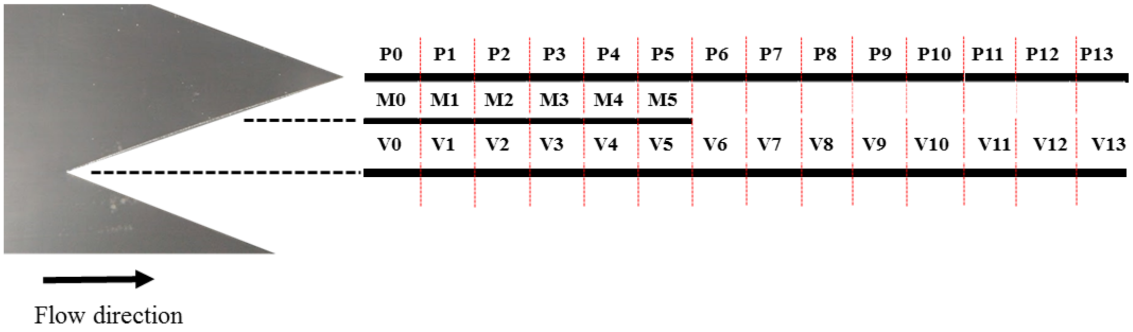

Figure 8: Schematic of all the locations where velocity data was collected.

4.3. Simulation Parameters

Specifics of the CFD package, mesher, and solvers used in this chapter can be found in Chapter III. The simulations in this chapter were built to match the geometry and flow physics of the experimental water tunnel testing. The inlet of the simulation was equivalent to roughly 150 mm downstream of the leading edge of the plate. The corresponding width was 300 mm, but the downstream length was increased to 1 m as simulations were not limited by the length of the tunnel test section. The first simulation was based on the flat plate model, while the subsequent runs were based on the flat plate with CVGs applied (all had the same domain size). Following the meshing guidelines discussed previously, all of the water tunnel based simulation domains had a total of 65 million cells. There were 3 different inlet velocity profiles used for the simulations, (0.6, 0.9, and 1.2 m/s). A time step of 2×10^{-5} seconds was used in this simulation. This ensures the stability of the simulations as it satisfies the Courant Friedrichs Lewy (CFL) condition. This condition is met when the Courant number,

$$C = \frac{u\Delta t}{\Delta x}, \tag{18}$$

is less than 1. See Table 2 to see full list of parameters.

Table 2: Geometry and flow properties of water tunnel simulations.

Parameter	Value	
H	1.5	mm
L	105	mm
W	76	mm
x	300	mm
Dimension	1 x 0.3 x 0.305	m
ρ	998	kg/m^3
μ	9×10^{-4}	Pa-s
U	0.6/0.9/1.15	m/s
δ	$2 - 2.5$	mm
Cell Count	65	million cells

4.4. Validation

4.4.1. Flat Plate

Validating computational simulations with experimental data is extremely important. But before analyzing and validating simulations with the CVG, it was important to ensure the selected methods and solvers adequately modeled the developing boundary layer over the flat plate. PIV data was taken at 158, 250, and 300 mm downstream location. While four different speeds were experimentally extracted, a tunnel speed of 1 m/s was used for validation. The experimental profile at 158 mm downstream of the leading edge was used as the inlet condition and the profiles at 250 mm and 300mm were used to validate the growth of the boundary layer. To analyze the boundary layers, both the vertical height and the velocity were scaled. The velocity (u) was scaled with the free stream velocity (U_∞), and the vertical height (y) was scaled with the 99% boundary layer thickness (δ). This allows for profiles to be compared even if they are at different downstream locations if they exhibit self similarity. Fig. 9 shows these scaled profiles extracted for the inlet, which appears to follow the laminar flat plate solution (Blasius solution) for all speed (i.e. they are self-similar). Fig. 10 shows a velocity contour plot of the developing laminar boundary layer that was modeled using these initial conditions.

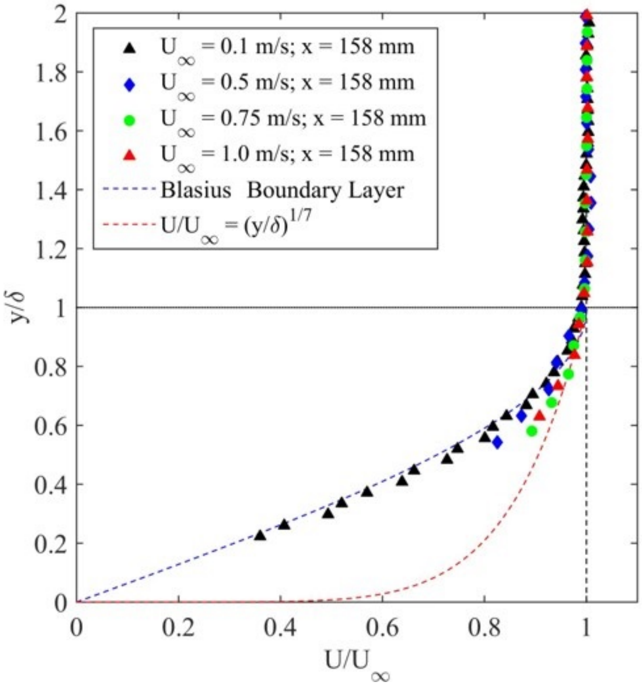

Figure 9: Experimental boundary layer profiles at x = 158 mm. Results are compared against the Blasius solution for a laminar flat plate and the turbulent 1/7th power-law velocity profile.

The next step was to validate the computational data collected with the experimental data. Fig. 11 shows the experimental and computational results as well as the exact solution for a laminar flat plate (Blasius solution). This figure does not show the full boundary layer as the experimental methods used to extract the data could not get data within $y/\delta < 0.3$. Nevertheless, looking at the experimental and computational results, the results match extremely well, despite the limitation of data in the near wall region. Based on this, the designed simulation was judged to adequately model the developing boundary layer.

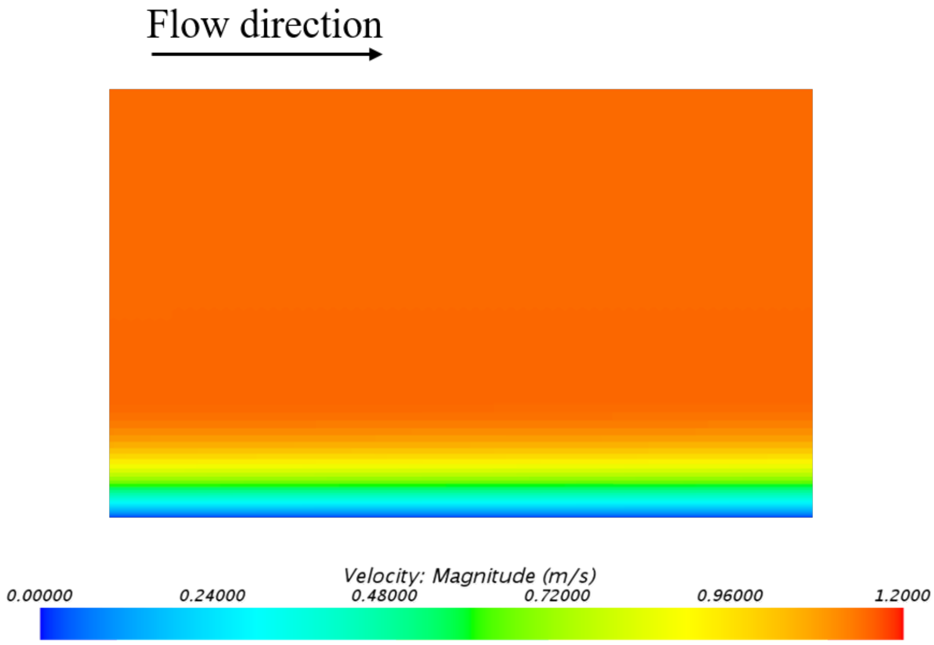

Figure 10: Contour plot of the velocity magnitude at $U_\infty = 1$ m/s, which shows the developing laminar boundary layer.

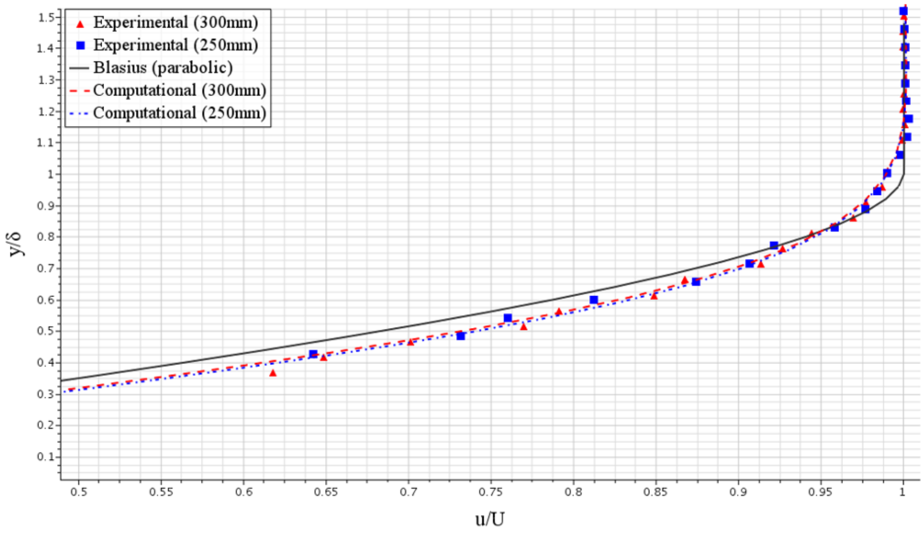

Figure 11: CFD and PIV comparison of y/δ (boundary layer scaled height) versus u/U (free stream scaled velocity) for a laminar boundary layer over a flat plate at two downstream locations.

4.4.2. *Flat Plate with CVG*

Following the modeling of the flat plate, the next step was to model the flat plate with CVGs attached. This was accomplished by cutting the CVG geometry out of the previous domain to create the 3D geometry of the backward-facing CVG step (Fig. 12). For this simulation, there were also three different inlet velocity profiles used (0.6, 0.9 and 1.15 m/s), all taken at the same 158 mm downstream location. The simulations explored how the CVG altered the flow by investigating changes in the velocity profiles as well as the distribution of wall shear stress. Velocity contour plots in Fig. 13 show the flow as it passes over a peak and a valley. This condition had a free stream speed of 1.15m/s inlet case and shows stark differences between the two spanwise locations (peak and valley). Fig. 14 shows a closer look at the reattachment region of the two steps and highlight their differences. Flow over the valley seems to have a more linear or convex reattachment region while the peak has a more traditional concave region that looks similar to a traditional BFS. Before this data was to be compared against experimental data, the mesh dependence of the solution had to be analyzed. Table 3 shows the 4 mesh iterations used to test this dependence with their corresponding shear diamond length (L_d) and boundary layer heights (δ_{99}). This table shows that at the most refined mesh, the solution is not dependant on the mesh sizing.

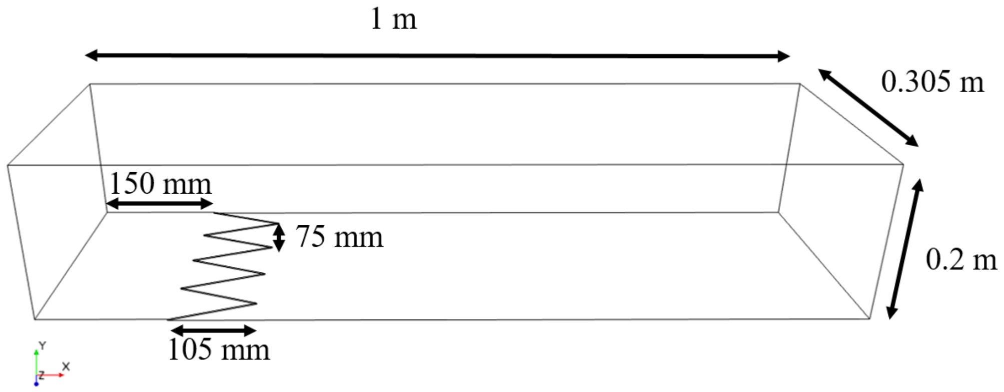

Figure 12: Simulation domain used to model the flow over a flat plate with CVGs. Flow is from left to right with the CVG making a 1.5 mm backward facing step.

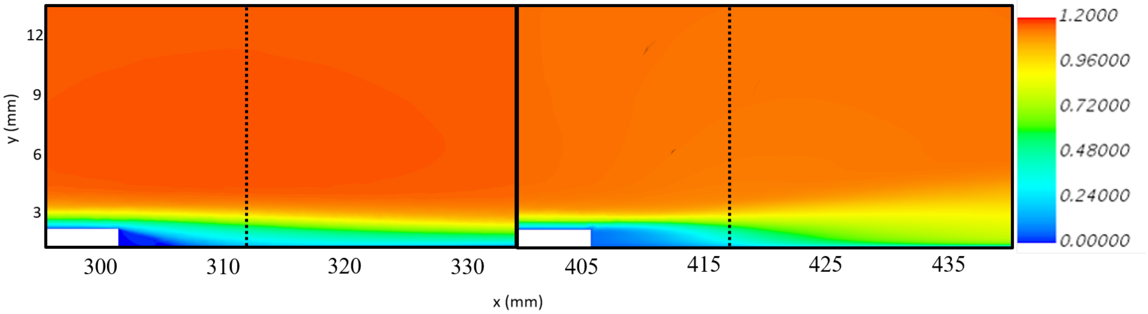

Figure 13: Contour plot of the velocity magnitude from the simulation showing flow over the step at the (left) valley location and (right) peak location. Flow is from left to right and the dashed lines indicate 7 step heights downstream of step.

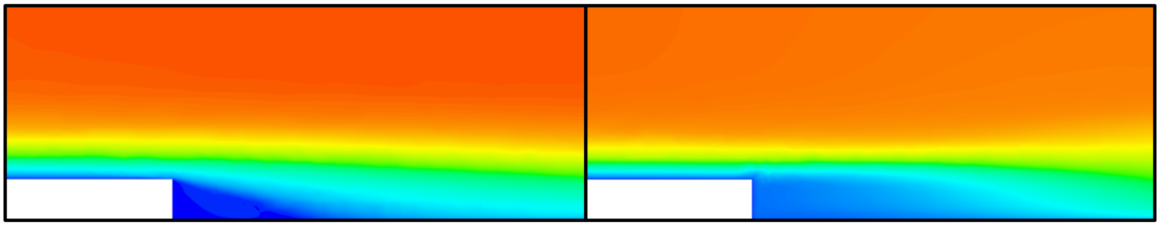

Figure 14: Contour plot of the velocity magnitude showing reattachment for (left) valley and right (peak).

Table 3: Values of L_d and δ_{99} showing mesh dependence of solution. Where P and V denote peak and valley respectively.

Mesh	L_d	δ_{99} @ $x = 0.1$ m	δ_{99} @ $x = 0.3$ m (V)	δ_{99} @ $x = 0.3$ m (P)
6,000,000	0.364 m	4.50 mm	5.10 mm	6.2 mm
12,000,000	0.324 m	3.90 mm	4.27 mm	5.15 mm
35,000,000	0.327 m	3.85 mm	4.24 mm	5.10 mm
65,000,000	0.327 m	3.83 mm	4.25 mm	5.10 mm

This data was then used for validating and verifying the simulations that utilized the CVG geometry. The starting point of this comparison involves the boundary layer characteristics. First, a qualitative comparison of velocity magnitude at the peak and valley locations was undertaken. Looking back at Fig. 13, there appears to be a very significant difference between the flow past the peak and the valley. While the flow past the two locations vary significantly they both appear to reattach at the expected 7 step heights (H) downstream of the step. This expected reattachment length holds true for both even though it appears that the flow past the peak is transitioning from laminar to turbulent while the flow past the valley remains laminar. This observation is very intriguing as the valley step is upstream of the peak step. Due to field of view limitations of the experimental setup, flow immediately downstream of the valley (flow between the valley and peak streamwise locations) could not be compared with experimental data. However, a comparison of data immediately downstream of the peak can be seen in Fig. 15 and shows that there is a very similar behavior in both of the images. Even with the lack of data right at the valley step, this comparison shows very strong similarities between the two which verify that the simulation is nominally modeling the flow.

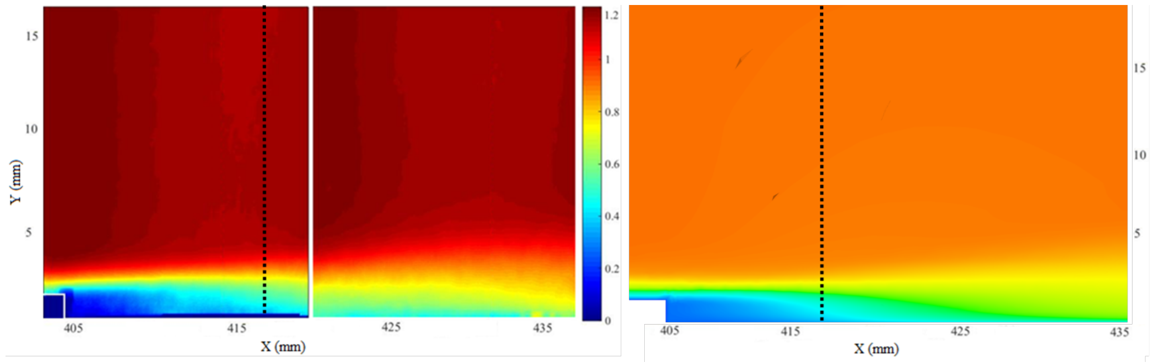

Figure 15: Velocity magnitude of flow over the peak for (left) experimental and (right) computational. Black dashed lines indicate 7 step heights downstream of the step.

Qualitative comparisons are insightful but to validate the simulations, quantitative comparisons are needed. This was done by analyzing the boundary layer shape factor for both experimental and computational results. The shape factor is defined in Eq. 6 as the ratio of displacement thickness to the momentum thickness. It is important to note that experimental data could not be taken directly downstream of the valley. Therefore, all of the plots contained in Fig. 16 start at the peak downstream location of 405 mm. The top row of Fig. 16 shows the shape factors for the valley. These plots show that at the lowest inlet speed (0.6 m/s), the flow remained laminar even past the downstream peak location. However, while both data sets (at 0.6 m/s) show that the flow remains laminar, the plots do not match. The experimental data is showing a transitional boundary layer and the computational data is showing transition. A likely cause of this is that computational simulations determine an exact location of transition, while real flows do not transition instantaneously. So, while these two data sets are not in complete agreement they both show that the flow is transitioning at this location. Fig. 17 shows the two boundary layers at this inlet speed further downstream where the peak location has transitioned. This plot shows how drastically different the two velocity profiles (peak and valley) are at the same downstream location. At 0.9 m/s, the shape factor shows that the boundary layer was transitioning right at the peak location. For this speed, Fig. 17 shows that while both of the

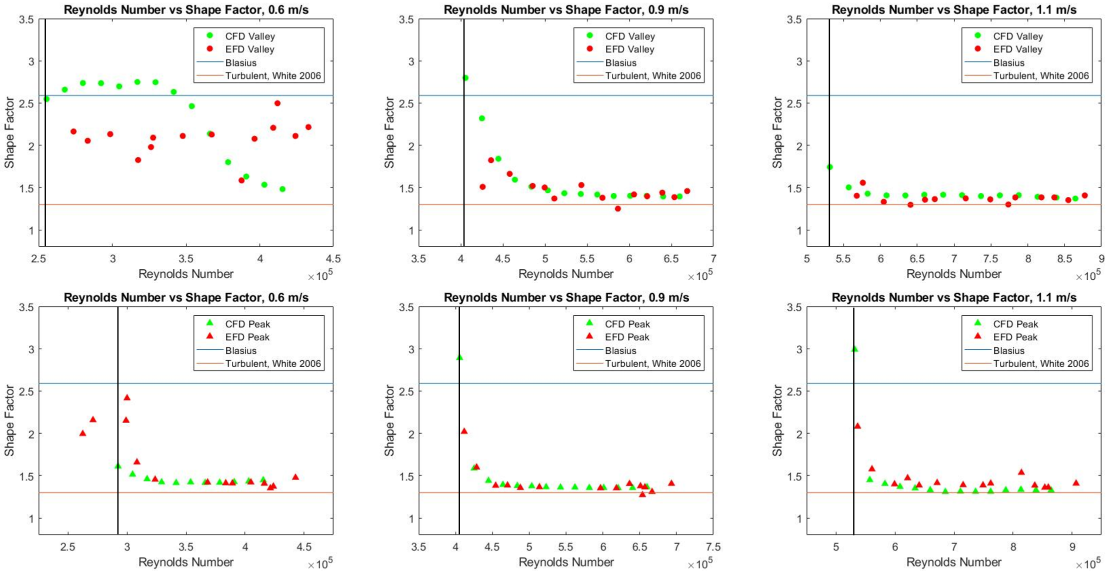

Figure 16: Boundary layer shape factor plots downstream of (top row) valley and (bottom row) peak at inlet speeds of (left column) 0.6 m/s, (middle column) 0.9 m/s , and (right column) 1.1 m/s compared against Blasius and turbulent literature values [27]. Black vertical line indicates location of the step and x-axis is Reynolds number based on downstream length (Re_x).

velocity profiles are turbulent, they are not identical. Thus, the CVG appears to impart a spanwise variation in the transition location, but also in the boundary layer characteristics after transition has occurred. In looking at this law of the wall plot, it is important to note that there is an offset in the log-law region. This offset is a known issue and is a result of the filtering that is inherent to LES due to its use of lower order schemes to solve the governing equations [26]. Lastly, at the highest speed of 1.15 m/s the flow seems to already be turbulent as it reaches the peak location. The bottom row of Fig. 16 shows that at all three of the measured speeds, the flow seems to transition to turbulence just past the peak step. In summary, at the three tested speeds, the shape factor of the boundary layer was dependant on the inlet speed past the valley, but not past the peak, showing that the CVG imparts a spanwise variation in the boundary layer characteristics.

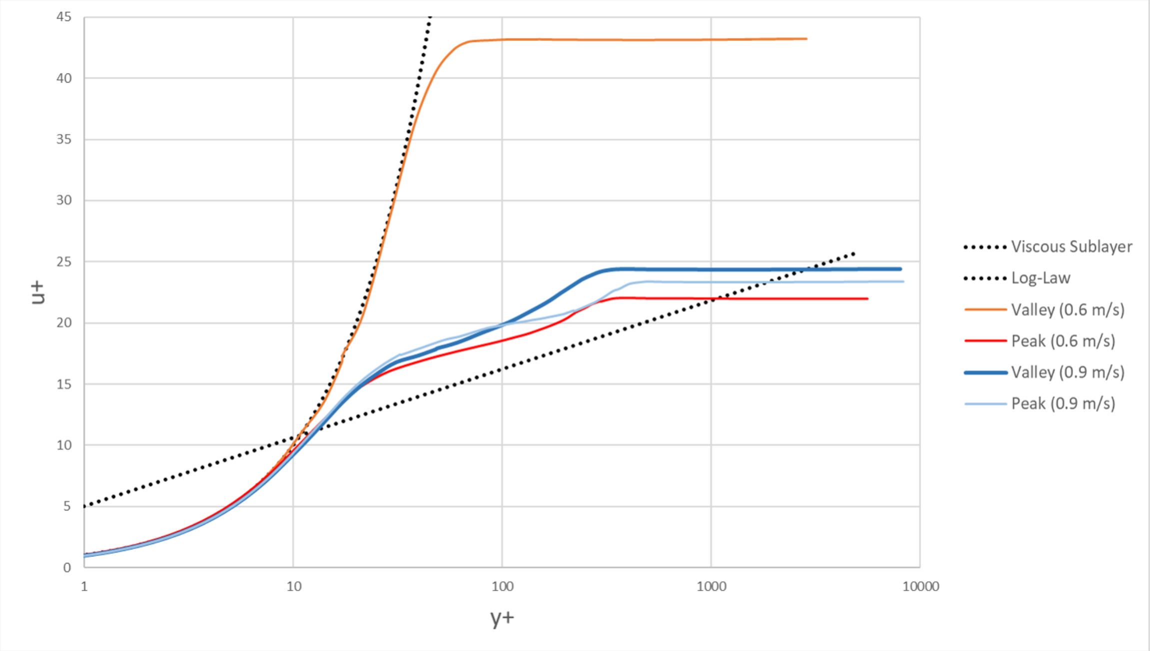

Figure 17: Law-of-the-wall velocity profiles for two inlet speeds (0.6 and 0.9 m/s) at the valley and peak 1 CVG length (105 mm) downstream of the peak step.

4.5. Computational Results

Following the validation and verification of the boundary layer characteristics, it concluded that the simulations could successfully model the flow past the CVG. This resulted in the ability to extract data from the simulations that, if solely relying on experiments, could not be obtained. The data that was extracted from the simulation following its validation was the wall shear stress for comparisons between the simulations and the flight test experiments. Wall shear stress was calculated and the resulting distribution is shown as a contour plot in Fig. 18. The first use of the wall shear data was to examine if patterns seen in the contour plots matched with the shape factor plots in Fig. 16. It was concluded that the observations in the shape factor are supported by the wall shear stress images shown in Fig. 18, which shows low shear diamonds occurring downstream of the valley. Based on the definition of wall shear,

$$\tau = \mu \frac{\partial u}{\partial y}, \tag{19}$$

a smaller velocity gradient in the y (vertical) direction results in a lower shear stress on the wall, resulting in a low wall shear stress in laminar regions and a higher shear stress in turbulent areas. An example of this conclusion can be seen in Fig. 19 where the boundary layer ($U_\infty = 0.6$ m/s) downstream of the valley is showing transition at the end of the shear diamond. Using this definition of the shear stress, as well as the qualitative comparison of Fig. 19, the shear diamonds match up well with the shape factor. The flow downstream of the valley is transitioning to high shear at the same locations where the shape factors were changing, as well as the shear stress being high past the peaks at all speeds.

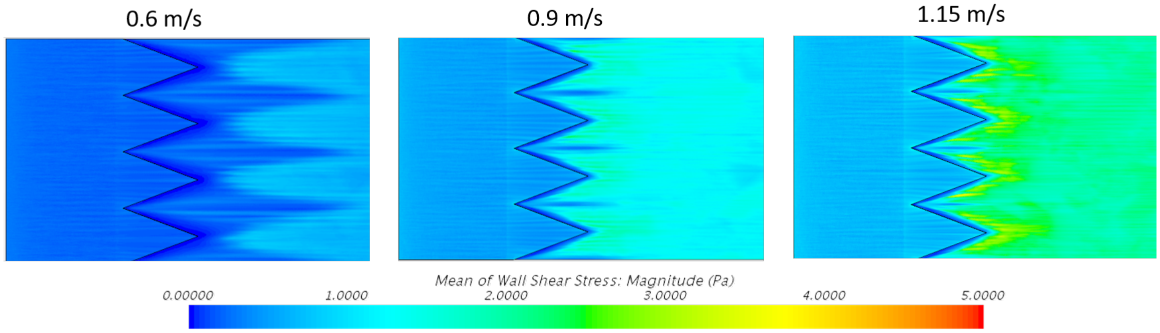

Figure 18: Contour plots of the wall shear stress magnitude for three different inlet speeds (0.6 m/s, 0.9 m/s, and 1.2 m/s). Flow is from left to right.

Figure 19: Contour plot of the wall shear and velocity magnitude showing the relation between the shear diamond and transition location at 0.6 m/s. Flow is from left to right and high shear values are shown in gray, while low shear is white.

Further investigation was performed with the wall shear stress data by comparing it to the flight tests performed by Edge Aerodynamix. First, qualitative comparisons indicate the low shear diamond feature was seen both in flight and the water tunnel. Fig. 20 shows a comparison of the diamonds between flight (b) and CFD (a & c). Images (b) and (c) show a strong similarity between flight testing and CFD, but this comparison is only qualitative due to the fact that the size of the diamonds can be adjusted with color scale. Next, looking at (a) and (c), a clear dependence on Re_H is shown. It appears the larger the value of Re_H, the smaller the shear diamond. Following this observation, a more in depth analysis of the diamond size was performed by comparing the ratio of the length of the diamond (L_d) to the length of the CVG geometry (L). This method was performed on all flight images as well as on the simulation data. Fig. 21 is an example of how these measurements were acquired. After examination it was found that not only was there a relationship between L_d/L and Re_H, but also the L/W ratio of the CVG. In Fig. 22, the ratio of the diamond length (L_d) to the CVG length (L) is plotted versus the ratio of the length (L) and the width (W). Data from the flight test and CFD are shown at the three different Reynolds numbers. Error

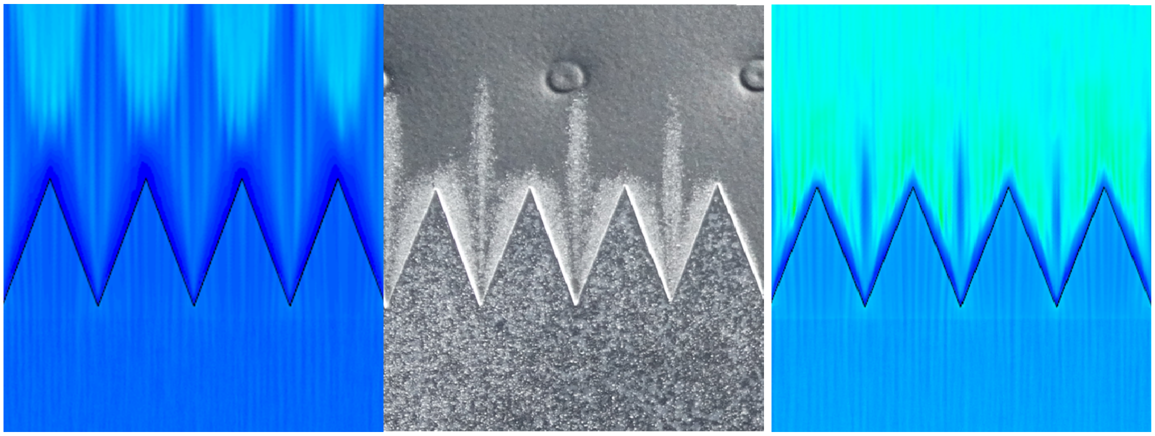

(a) Re_H = 900 (CFD) **(b) Re_H = 1300 (flight test)** **(c) Re_H = 1350 (CFD)**

Figure 20: Wall shear stress comparison at varying Re_H: (a) Re_H = 900, (b) Re_H = 1300, and (c) Re_H = 1350)

bars on the flight test data are the standard deviation from the multiple CVG measurements at the same L/W value. It is not surprising the the CFD and the flight scale data are different, even at the same Re_H, since the flight scale length is time sensitive and the CFD can be adjusted based on threshold levels. However, both flight and CFD show that L_d/L decreases as Re_H increases. Furthermore, the flight test data shows an L/W dependence with L_d/L decreasing with increasing L/W. Fitting the data to a power-law function results in $L_d/L = 3.1Re_H{}^{-5/8}$, $L_d/L = 2.6Re_H{}^{-5/8}$, $L_d/L = 1.9Re_H{}^{-5/8}$ for Re_H = 1360, 1460, and 1655, respectively. All of these fits are plotted in Fig. 22 and the percent difference between each of the experimental data points and their corresponding predicted value can be seen in Fig. 23. These plot shows that as the L/W ratio of the CVG or the Re_H increases, the size of the shear diamond scaled by the CVG length decreases.

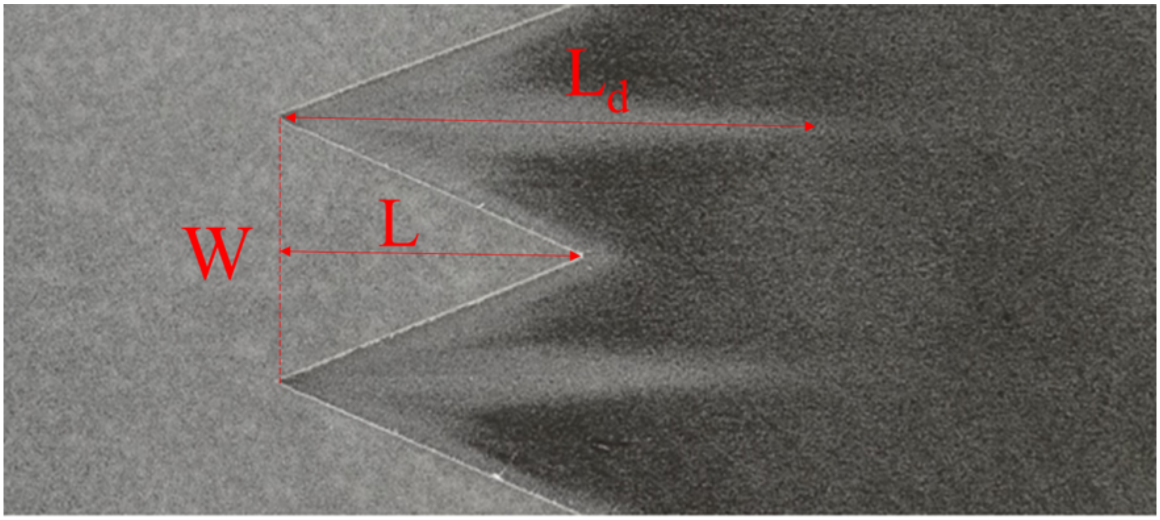

Figure 21: Visual of how the shear diamonds were sized

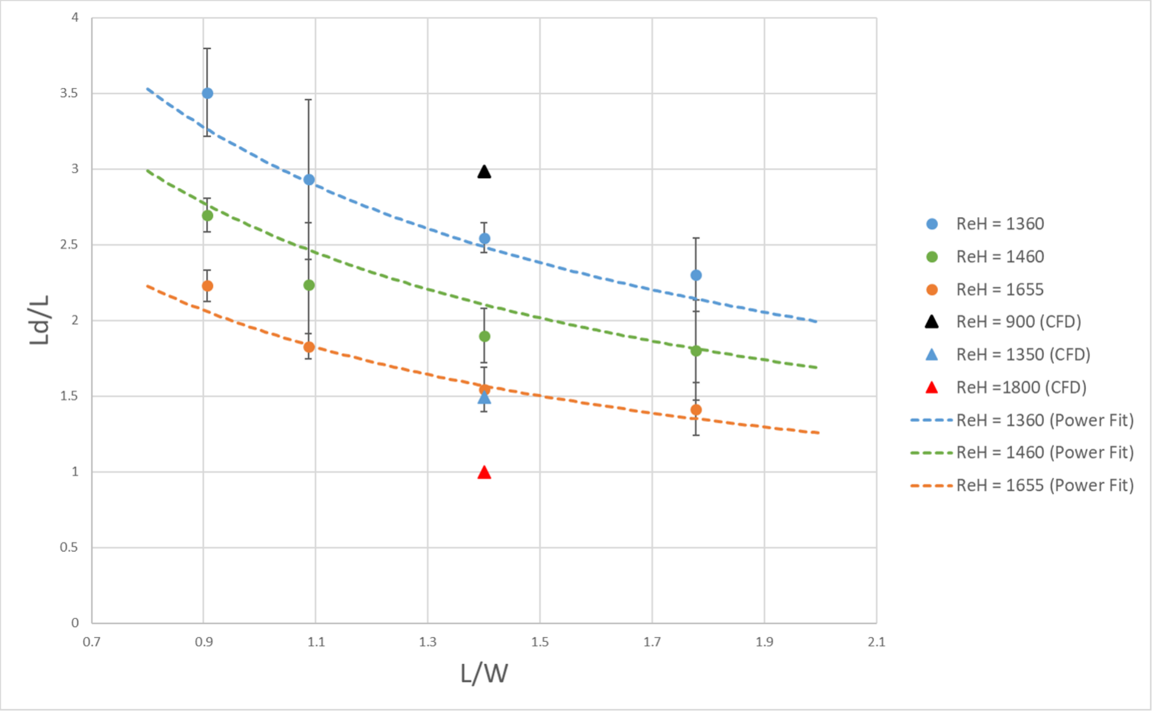

Figure 22: Shear diamond length (L_d) scaled with the CVG length (L) plotted versus the CVG L/W ratio (and Re_H). Dashed lines are the power-law fit for each Re_H.

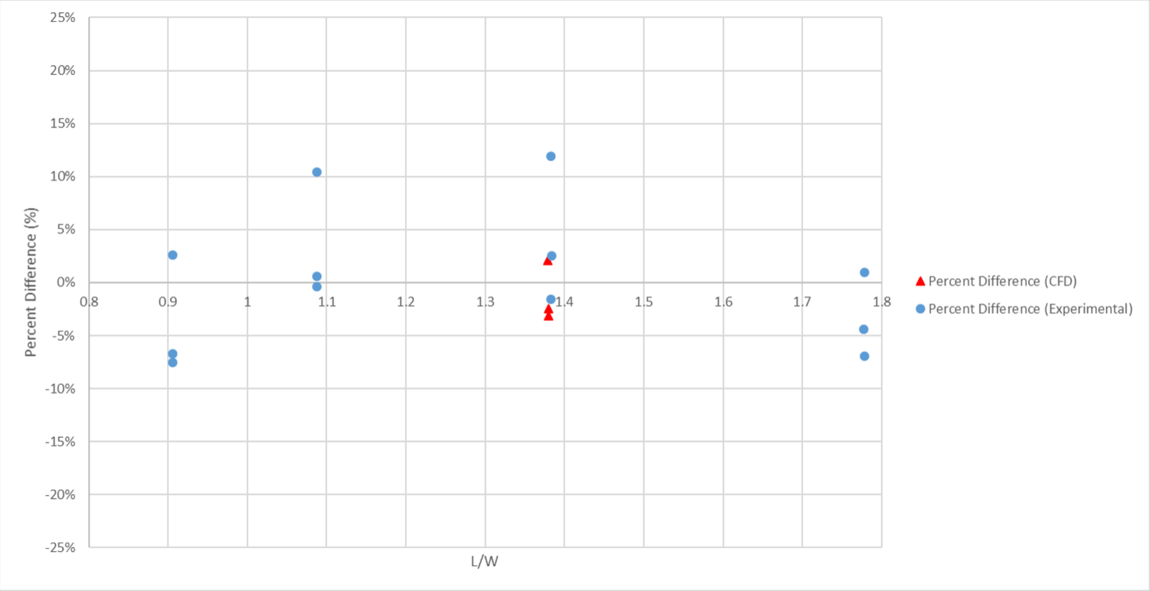

Figure 23: Percent difference of fitted data versus actual data for CFD and experimental.

The next data set that was extracted from these validated simulations was the skin-friction coefficient (C_f), defined by,

$$C_f = \frac{\tau_w}{\frac{1}{2}\rho U_\infty^2}. \tag{20}$$

It was vital to investigate how the CVG impacted skin friction as it is a direct component of drag. The flow features seen in the skin friction contour plots ((Fig. 24) look identical to those in the wall shear (Fig. 18), but the magnitudes will vary. This is due to Eq. 20, where the wall shear stress is scaled by the freestream velocity (U_∞). Investigating these plots, it appears that the lowest speed (0.6 m/s) has the largest areas of high shear. This speed had the largest shear diamonds, meaning the largest spanwise variation in transition, which indicates that the regions of highest shear reside in regions of transition. This observation indicates that more prominent the features are in the skin friction, the higher the value of C_f. Performing a surface average on the plate downstream of the CVG shows a similar pattern with average C_f values of 0.0029, 0.0028, 0.0027 for 0.6, 0.9, and 1.15 m/s respectively. The conclusions from the skin friction show a similar pattern to observations made in

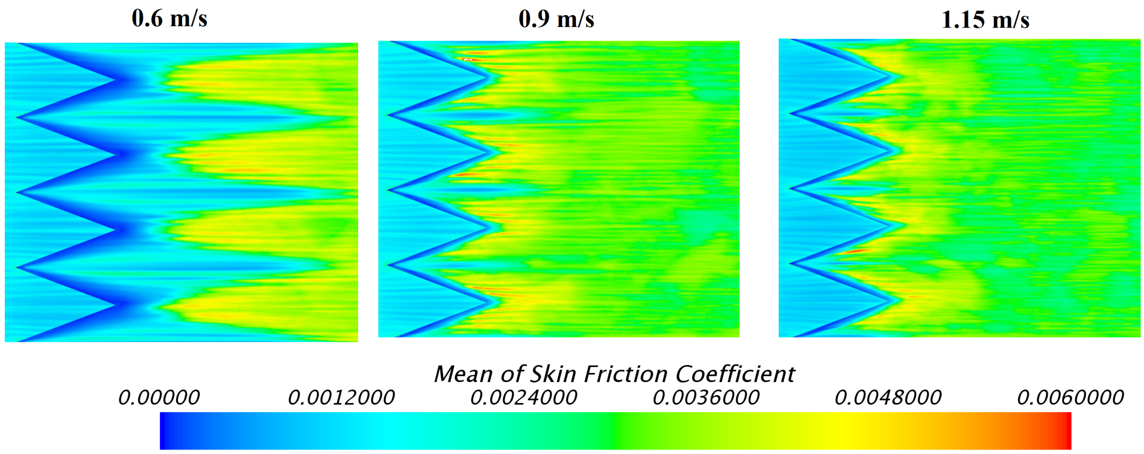

Figure 24: Contour plots of the wall shear stress magnitude for three different inlet speeds (0.6 m/s, 0.9 m/s, and 1.15 m/s). Flow is from top to bottom.

The final sets of data that were extracted from these validated simulations were the Q-criterion and streamlines. The Q-criterion defines a vortex as,

$$Q = 0.5(|\Omega^2| - |S^2|) > 0, \tag{21}$$

where Ω is the vorticity and S is the strain rate. This equation states that a vortex exists when the difference between the vorticity and strain rate is greater than zero [28]. Due to the use of three different inlet speeds (0.6, 0.9, 1.15 m/s) a scaled threshold was set so that a comparison could be made about the location of structure formation (as a higher velocity would inherently generate more vorticity). To accomplish the visualization of the vorticty formation, isosurfaces were utilized (isosurfaces are 3D surfaces that are only present when the value of Q-criterion was above the threshold), allowing for a 3D visual representation of the vorticity. Fig. 25 shows the Q-criterion isosurfaces for all three inlet speeds. This figure shows that the vortex formation for these simulations is tied to the transition locations with the strongest features located where the flow is becoming turbulent. These figures match up extremly well with the wall shear plots that show that at lower inlet speeds, the spanwise variations in the fluid structures are more apparent.

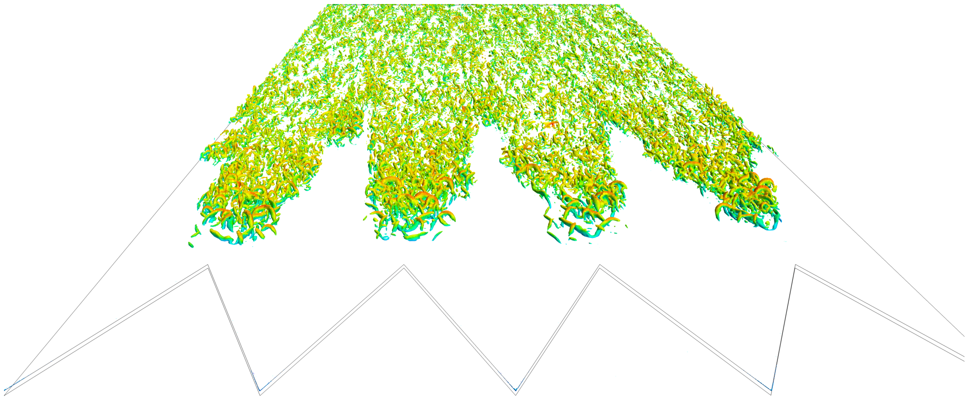

(a) 0.6 m/s

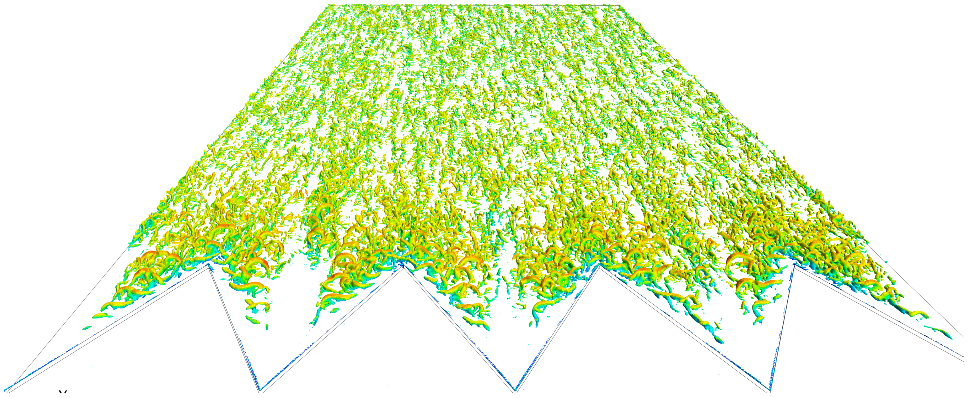

(b) 0.9 m/s

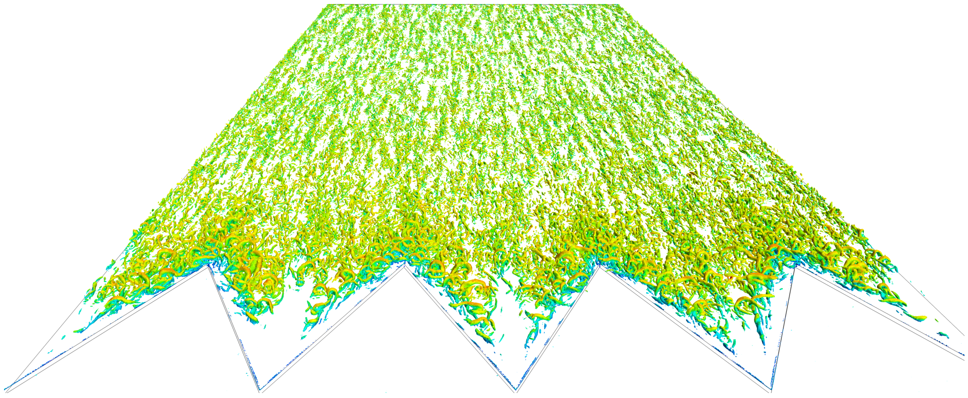

(c) 1.15 m/s

Figure 25: Isosurface of the Q-criterion for the inlet speeds of (top) 0.6 m/s, (middle) 0.9 m/s, and (bottom) 1.15 m/s.

Next, Fig. 26 shows streamlines as they pass over the CVG for the simulation with an inlet speed of 0.6 m/s. A streamline is a flow line that shows how a fluid particle travels through the system. This figure shows streamlines that are seeded from the wall as well as from inside the boundary layer (1.5 mm off of the wall) to show how the CVG effects flows at different vertical locations. These images show how the flow in certain regions interact with the CVG and the color scale is the wall distance of the streamline. The top picture shows that the flow in the near wall region is directed to the peaks of the CVG and almost none of the flow travels directly off of the valley. The bottom image shows streamlines that are seeded from inside the boundary layer and show that as they go over the peak, the fluid is shifted up, and as the flow passes over the valley, the flow is driven down. This rise off of flow over the peak is supported by the fact that the near wall flow is drawn to the peak. This causes an increase in the amount of flow at the peak which, in turn, causes the boundary layer to rise. Also, due to the lack of flow coming from the near wall region to the valley, flow is pulled down from the boundary layer to the near wall region. This region where the flow is pulled down lines up with the low shear diamond feature previously discussed in this section and it is where the flow remains locally laminar.

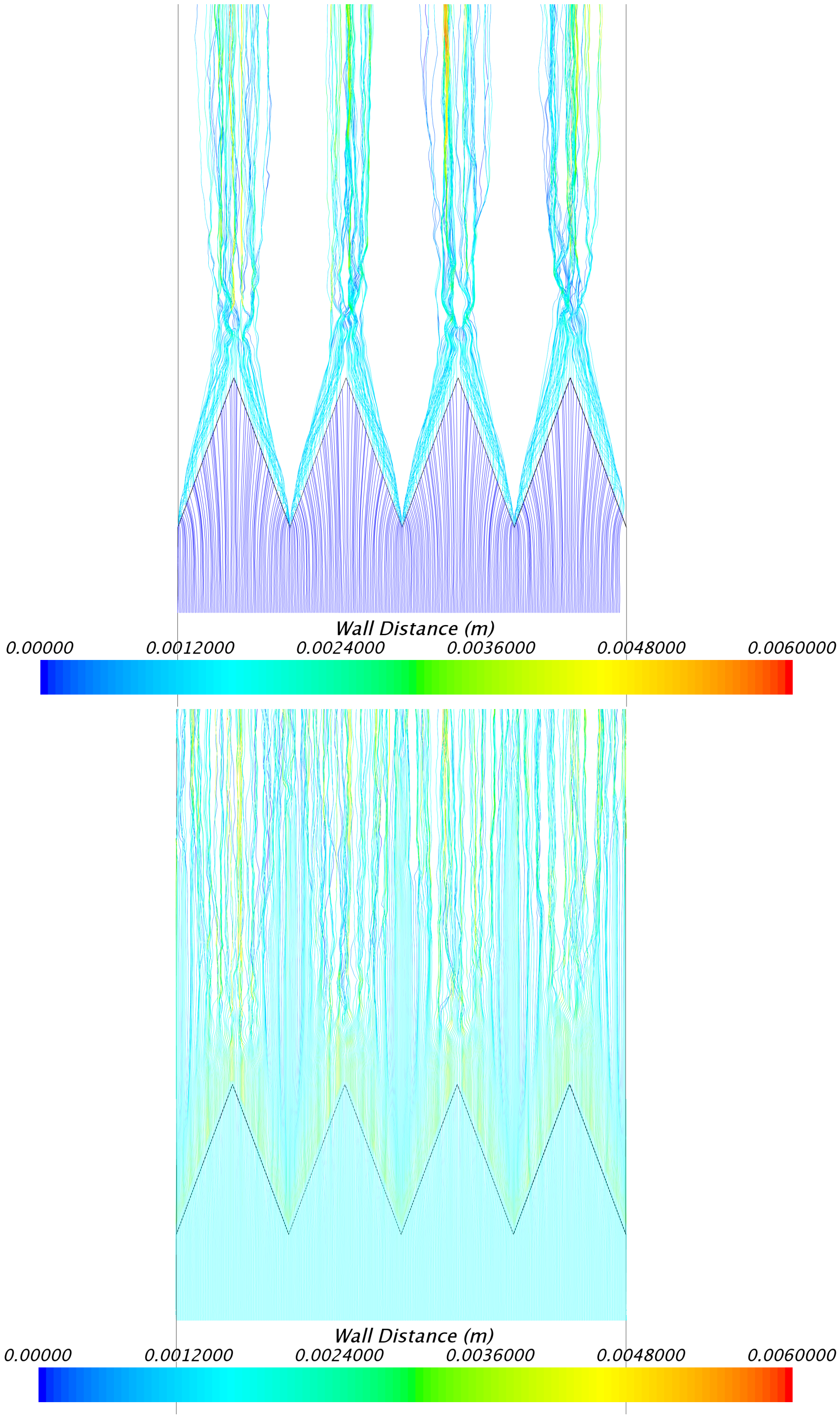

Figure 26: Streamlines that are seeded from the (top) wall and (bottom) inside the boundary layer showing how the flow moves past the CVG.

4.6. Conclusion

Simulations were built to match water tunnel testing operation conditions with the goal of replicating results that were seen in both water tunnel testing and flight testing. The first of these simulations was the validation of a flat plate, achieved by comparing the growth of a laminar boundary layer using experimental data as the initial conditions. Following this, simulations were set up with the CVG geometry ($L = 105$ mm, $W = 76$ mm, and $H = 1.5$ mm) that was of same domain size (1 m long by 0.3 m wide) as the flat plate simulation. These simulations were run at three different inlet conditions; 0.6, 0.9, and 1.15 m/s. The CVG simulations were verified by examining the velocity distribution downstream of the peak and the valley and comparing to PIV results. These simulations were then validated with water tunnel and flight test data by quantitatively comparing the boundary layer and wall shear characteristics. Four primary conclusions can be made from these simulations and comparisons:

1. The flat plate simulation was validated as the boundary layer profile matched experimental data, which followed closely to the Blasius laminar solution.
2. The CVG simulations were verified and validated by comparing boundary layer characteristics with the experimental results as well as analyzing the wall shear stress distribution compared with flight scale observation.
3. The CVG imparts spanwise variation in the wall shear stress of the flow.
4. The wall shear diamonds were found to be a repeatable feature in both CFD and flight testing. These features have both a L/W and Re_H dependence.

CHAPTER V

SIMULATION II: FLIGHT SCALE

5.1. Simulation Parameters

Two sets of simulations were developed to study CVG behavior at flight scale. The first set of simulations in this section were built to analyze the flow physics on an in flight wing, with the explicit goal to match the in flight flow properties that would be seen on the Boeing 737 at the CVG's application location (10% cord). Due to the nature of the CVG's size, the simulations require high spatial resolution at the wall. The CVG sizes for these simulations are provided in Table 4. Each simulation had a width of 4 full CVG widths (W) and a total of 4 different CVG geometry configurations (varying L/W) were used. A flat plate and a backward facing step (BFS) were also simulated for comparison. This was done to examine not only the effect of the L/W ratio on flow properties past the CVG, but also how the CVG compares to other geometries. Due to these simulations being based on the in flight physics, the fluid properties of air at 10,000 m (cruise altitude) were used. It is important to note that while Boeing 737 aircraft cruise at around Mach 0.7, the flow is locally supersonic in the region that the CVG is applied (see Fig. 3 for location on the wing). The individual flow and geometry properties are given in Table 5 and further details regarding the simulations can be found in the Computational Methods chapter (Chapter III.).

Table 4: Geometry and flow properties of flight scale simulations.

	L (m)	W (m)	H (m)	L/W ratio
CVG-1	0.0267	0.0193	0.367	1.36
CVG-2	0.0134	0.0096	0.367	1.36
CVG-3	0.0267	0.0096	0.367	2.72
CVG-4	0.0134	0.0193	0.367	0.69

Table 5: Geometry and flow properties of flight scale simulations.

Parameter	Value	
H	0.367	mm
L	$13.35 - 53.4$	mm
W	$9.65 - 38.6$	mm
x	100	mm
Dimension	0.45 x 0.03-0.14 x 0.03	m
Altitude	$10,000$	m
ρ	0.467	kg/m^3
μ	1.46×10^{-5}	Pa-s
U	400	m/s
δ	7	mm
Cell Count	$30 - 50$	million cells

The second set of simulations were built based on an experiment conducted by NASA on transonic wings with an aft facing step [29]. These experiments utilized the RAE 2822 airfoil and looked at the pressure, drag, and lift coefficients with varying step scaling and locations. The purpose of these simulations were to validate a full 2D airfoil simulation (with a step), get crucial data for comparison to the Boeing 737 based simulations, and quantify the effect of a aft facing step on an airfoil. These simulations were all 2D simulations utilizing a RANS (k-ω) solver with inlet and boundary conditions based on the experimental testing. The mesh was made utilizing an unstructured polyhedral mesh with the implementation of a table based mesh adaption. This mesh adaption found regions with a high density gradient and decreased the mesh size, which allowed the ability to capture the supersonic features in the flow. The individual geometry and flow properties are given in Tables 6 and 7.

Table 6: Geometry and flow properties of 2D RAE 2822 simulations.

Parameter	Value	
α	2.31	degrees
H	3	mm
Cord	1	m
Dimension	130 x 60	m
ρ	1.48	kg/m^3
μ	5.33×10^{-5}	Pa-s
U	0.729	Mach
Cell Count	5	million cells

Table 7: Geometry and flow properties of 2D BFS and ramp simulations.

Parameter	Value	
H	2	mm
x	100	mm
Dimension	1 x 2	m
Altitude	$10,000$	m
ρ	0.467	kg/m^3
μ	1.46×10^{-5}	Pa-s
U	400	m/s
δ	7	mm
Cell Count	3	million cells

5.2. Results and Discussion

5.2.1. Wall Shear Stress

As concluded by the water tunnel simulations, the CVG imparts spanwise variation in the wall shear stress of the flow in the subsonic regime. Therefore, it was important to see if this held true in the supersonic regime (flight scale). Also, since the goal of this technology is to decrease the fuel consumption of an aircraft, it was vital to quantify the impact these CVGs had on the overall skin friction drag (wall shear stress). Thus, several different simulations were run and time averaged wall shear stress was captured. The wall shear stress was calculated using shear stress relationship (Eq. 19). Due to all of the flight scale simulations having the same free stream speed, wall shear stress was converted to skin friction coefficient (Eq. 20) and was found to have identical contour plots. These results are found in Figs. 27 and 28, including two CVG geometries as well as a BFS. This data was used to analyze the spanwise variation of the wall shear past the CVG in comparison with a BFS and to determine how the wall shear modification varied with CVG L/W.

Next, spanwise averages were taken (vertical slices of Fig. 27) to examine the downstream dependence of the wall shear, which is shown in Fig. 29.

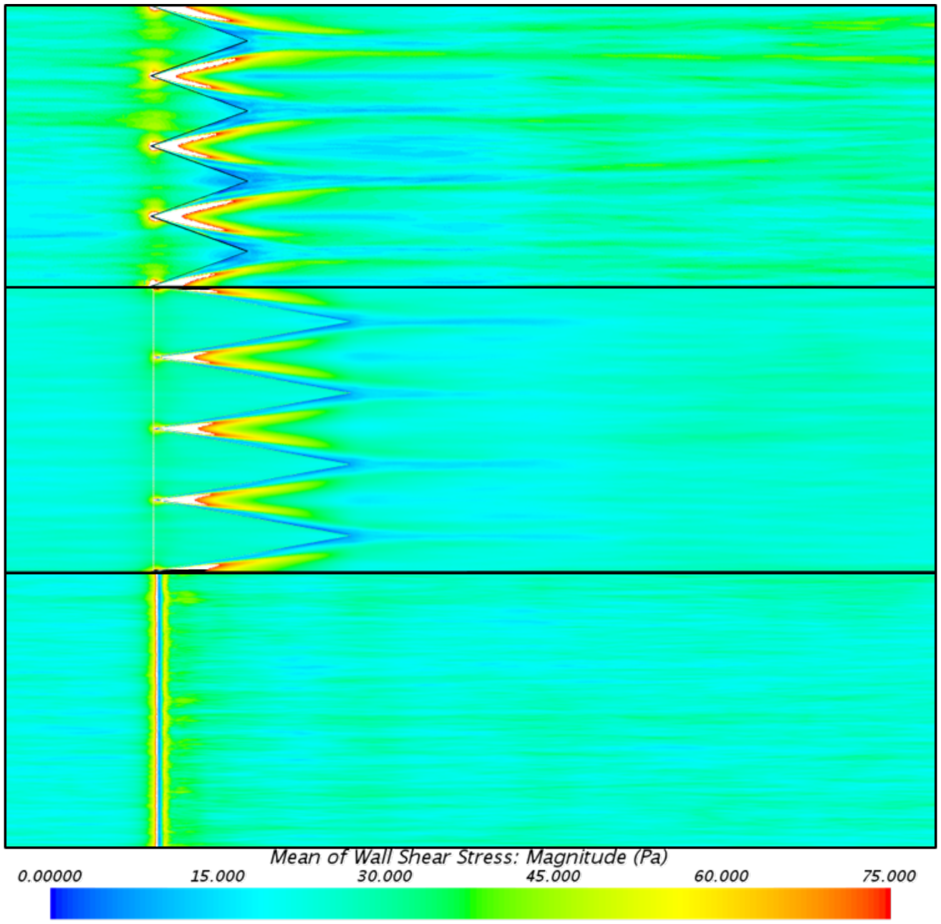

Figure 27: Streamwise and spanwise distribution of the time averaged wall shear stress for the (top) CVG with $L/W = 1.36$, (middle) CVG with $L/W = 2.72$, and (bottom) BFS located at the CVG valley location. Flow is from left to right at Mach 1.34.

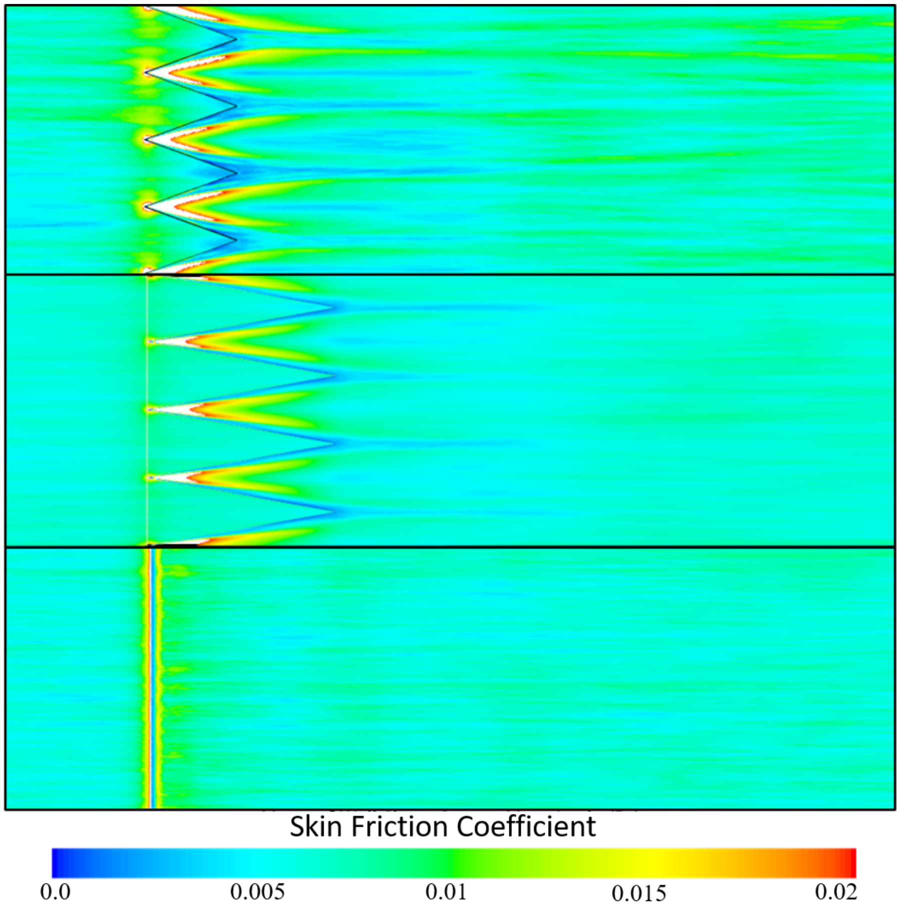

Figure 28: Streamwise and spanwise distribution of the time averaged skin friction coefficient (C_f) for the (top) CVG with $L/W = 1.36$, (middle) CVG with $L/W = 2.72$, and (bottom) BFS located at the CVG valley location. Flow is from left to right at Mach 1.34.

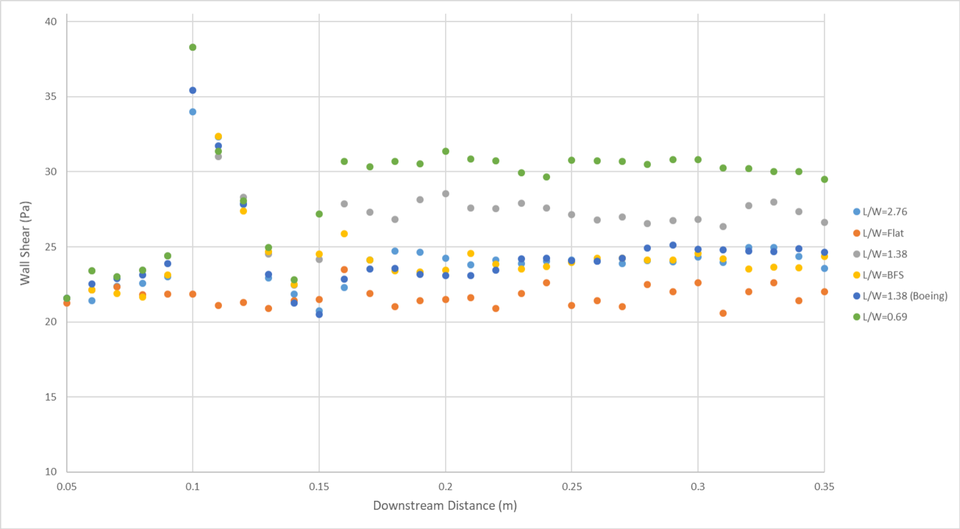

Figure 29: Comparison of time averaged wall shear vs downstream distance at Mach 1.34.

The first flow characteristic investigated was if wall shear stress modification seen in the laminar water tunnel based simulations were also seen in the flight scale turbulent simulations. Figures 18 and 27, illustrate the differences for the two conditions. In both figures, evidence suggests that the CVG imparts spanwise variation in the wall shear. However, they do not follow the same pattern. The laminar, subsonic case has a low shear diamond that forms between the CVGs while the flight case (turbulent and supersonic) shows a high shear feature between the CVGs with low and high shear streaks persisting downstream from the peaks. This is likely due to the drastically different flow regimes where the CVGs reside. The laminar case has diamonds that form in the regions where the CVG causes spanwise variation in the shape of the boundary layer (laminar vs turbulent), while the flight scale CVGs are turbulent everywhere and are in a supersonic flow. Due to this high Mach number, the flight scale CVGs see an expansion fan over the step. This increase in Mach (due to the fan), as well as the compression of the boundary layer seen in Fig. 30 is conjectured to be the cause of these high shear features. These flight features also appear to be related to the L/W ratio of the CVG as the $L/W = 2.72$ in Fig. 27 shows weaker and smaller features than that of the $L/W = 1.36$ CVG. This variation between different L/W ratios CVGs can also be seen in Fig. 29, where a relationship is indicated between L/W and downstream (spanwise averaged) wall shear stress. It appears the higher the L/W CVG ratio, the lower the average wall shear as well as less prominent spanwise features and streaks. Therefore, it can be concluded that the flight scale CVGs also impart spanwise variations in the wall shear that is dependent on the L/W ratio. However, this distribution of wall shear stress differs from the laminar subsonic case.

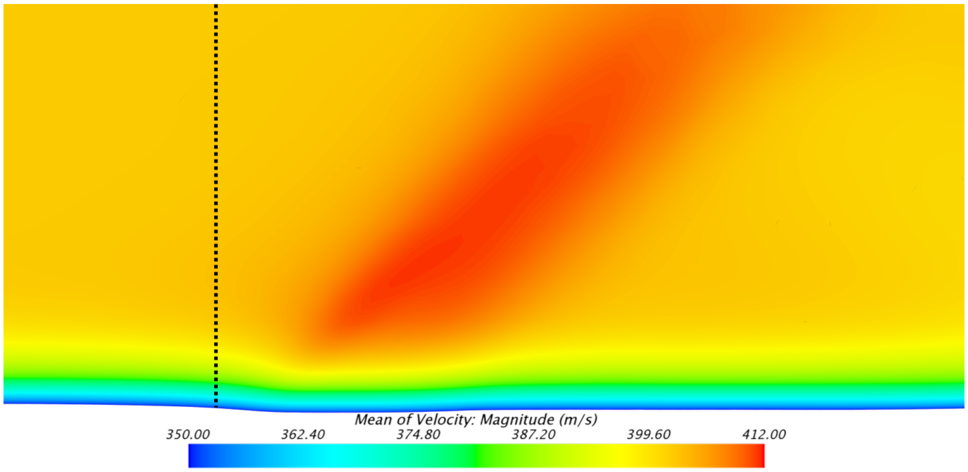

Figure 30: Velocity contour plot showing the expansion fan that forms over the CVG step. The dashed black line indicates the valley step location.

5.2.2. Vortex Formation and Streamlines

As the name CVG (Conformal Vortex Generator) implies, it was important that the vortex formation off the CVG be investigated. This was done by utilizing the Q-criterion. The Q-criterion defines a vortex as,

$$Q = 0.5(|\Omega^2| - |S^2|) > 0, \tag{22}$$

where Ω is the vorticity and S is the strain rate. This equation states that a vortex exists when the difference between the vorticity and strain rate is greater than zero [28]. However, since this flow is highly turbulent, there is quite a bit of vorticity in the flow, making it difficult to distinguish between just turbulence and the dominant coherent vortices of interest. Therefore, a threshold was set so that only regions of high Q-criterion were shown to better allow for visualization of the vortex structures being produced by the CVGs. To accomplish this, isosurfaces were utilized (isosurfaces are 3D surfaces that are only present when the value of Q-criterion was above the threshold), allowing for a 3D visual representation of the vortex. Two examples of this can be seen in Fig. 31 and Fig. 32. These two figures show an example of the Q-criterion isosurfaces downstream of a BFS and a CVG. These cases were run at the same conditions, with an inlet Mach number of 1.34. It was also of importance to see how this generation of vortices changed between the peak and valley of the CVG simulation. To visualize this, 2D isosurface planes were generated at the peak and valley spanwise locations which can be seen in Fig. 33.

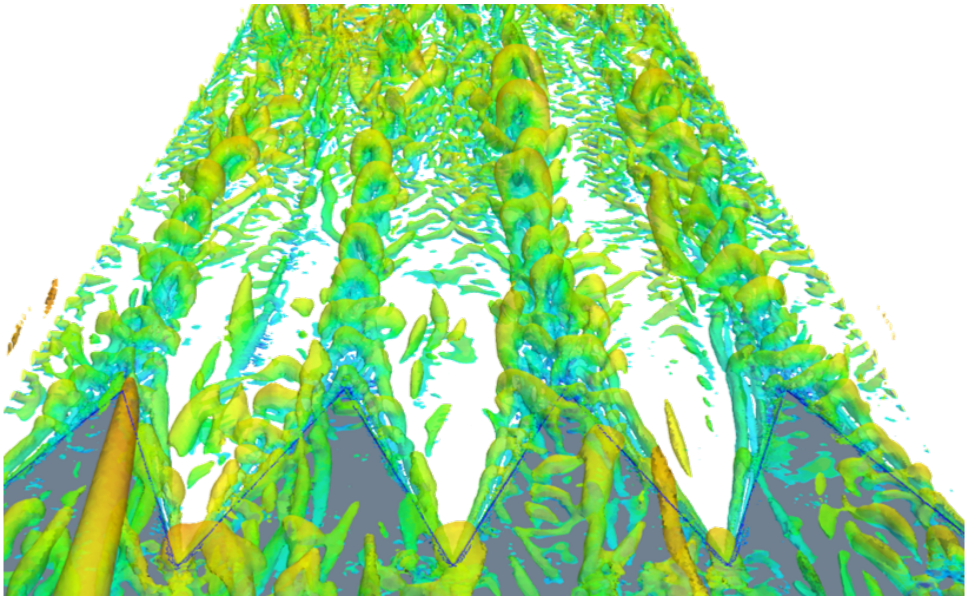

Figure 31: Q-criterion isosurface showing vortex formation past the CVG.

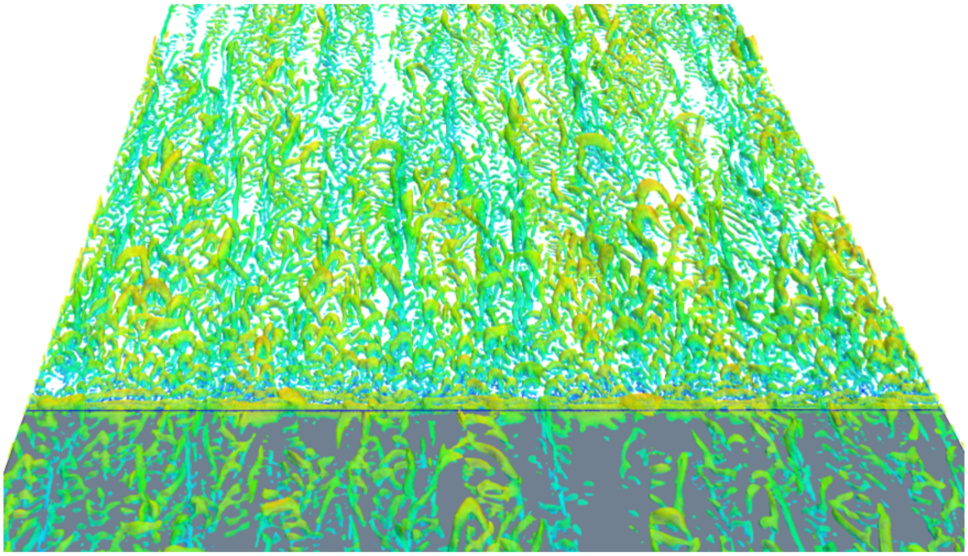

Figure 32: Q-criterion isosurface showing vortex formation past a BFS.

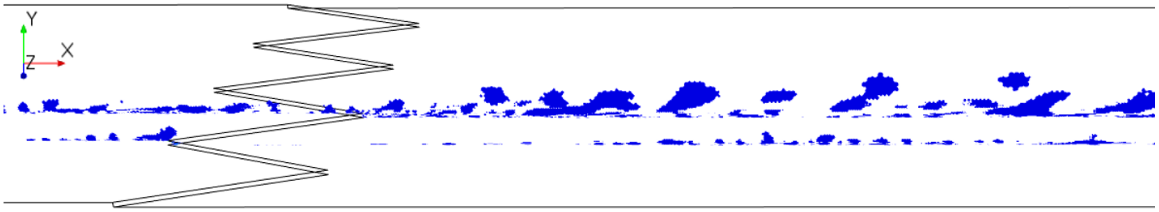

Figure 33: Q-criterion isosurface planes showing vortex formation past a peak and valley of CVG.

The spanwise variation in wall shear, discussed in the previous section, is supported further by the Q-criterion isosurfaces. Fig. 31 shows hairpin like vortex structures being shed off of the CVG peaks while there is minimal vortex formation off of the valleys. Comparing this figure to Fig. 27, it appears that the locations of vortex formation are in the areas of high wall shear, with the center of these hairpin structures located in the same areas as the low shear streaks. This observation is also seen in [30], where high friction (or wall shear) regions are formed at the legs of the hairpin vortices when they are generated in the near wall region. This provides evidence that the CVG is energizing the boundary layer and generating coherent vortex features. For comparison, see Fig. 32, which shows the same isosurface downstream of the BFS. This figure shows that with a traditional BFS, small uniform vortex formation downstream of the step occurs but with a CVG, strong vortex formation occurs primarily downstream of the peak with regions of low vorticity in between. The difference in the spanwise vortex formation of the CVG is seen more clearly in Fig. 33, where isosuface planes demonstrate the size difference in the vortices off of the peak of the CVG versus the valley.

Next, Fig. 34 shows streamlines as they go over the CVG, both seeded from the wall and inside of the boundary layer. First, comparing these images to Fig. 26 (subsonic simulations), there appears to be very similar behavior. The flow from the wall is directed towards the peak with almost none of the flow going over the valley and the flow in the boundary layer is driven up past the peak and driven down past the valley. These observations match up with the wall shear and vortex formation observations. The hairpin vortex features are forming in the same locations in which the flow is drawn from the wall and pulled up into the boundary layer and the regions of low vortex formation line up with the regions where the flow is drown down into the near wall.

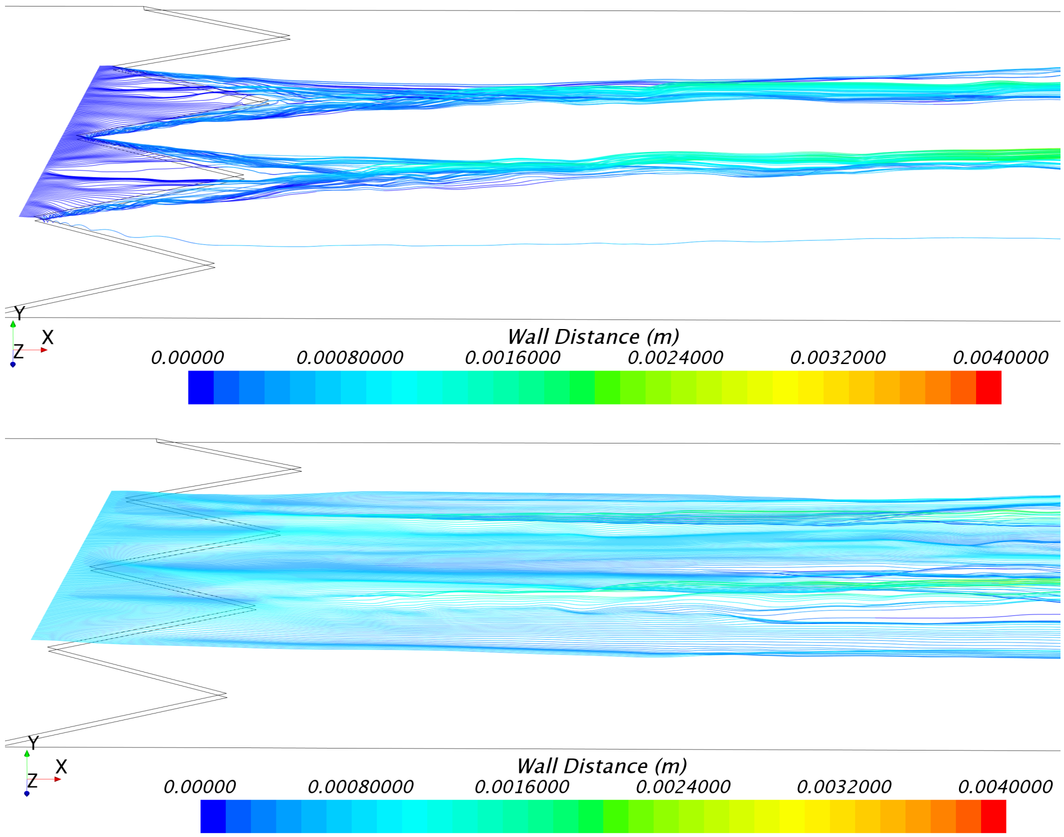

Figure 34: Streamlines that are seeded from the (top) wall and (bottom) inside the boundary layer showing how the flow moves past the CVG.

5.2.3. 2D RAE 2822

The 2D RAE 2822 simulation had the purpose of validating a small scale step on an airfoil. This step is vital as there is no validation data for a CVG flight case. The experiment chosen examined the effect of an aft facing step (in the same cord position as the CVG) on an airfoil. To compare this simulation to the experimental data, coefficients of pressure (C_p), normal force (C_n), and drag (C_d) were examined. Comparisons of C_n and C_d can be seen in Table 8 and to see a comparison of the C_p plot, see Fig. 35. A Mach number contour plot was also created to visualize the flow over the airfoil, this can be seen in Fig. 36.

Table 8: Comparison between CFD and Experimental Results.

Parameter	CFD	Experiment	%-Difference
C_n	0.736	0.743	0.95%
C_d	0.0128	0.0127	0.8%

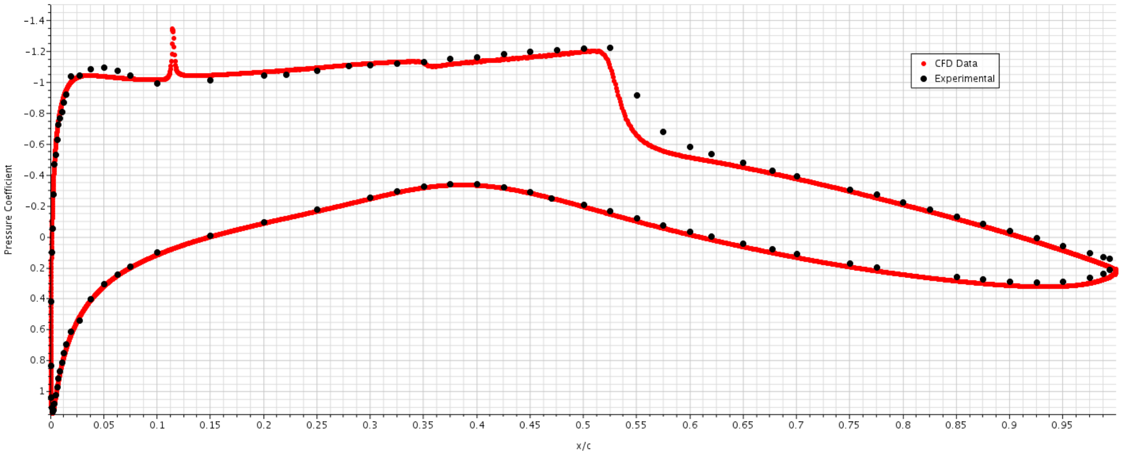

Figure 35: Plot showing pressure coefficient versus cord location at top and bottom of surface.

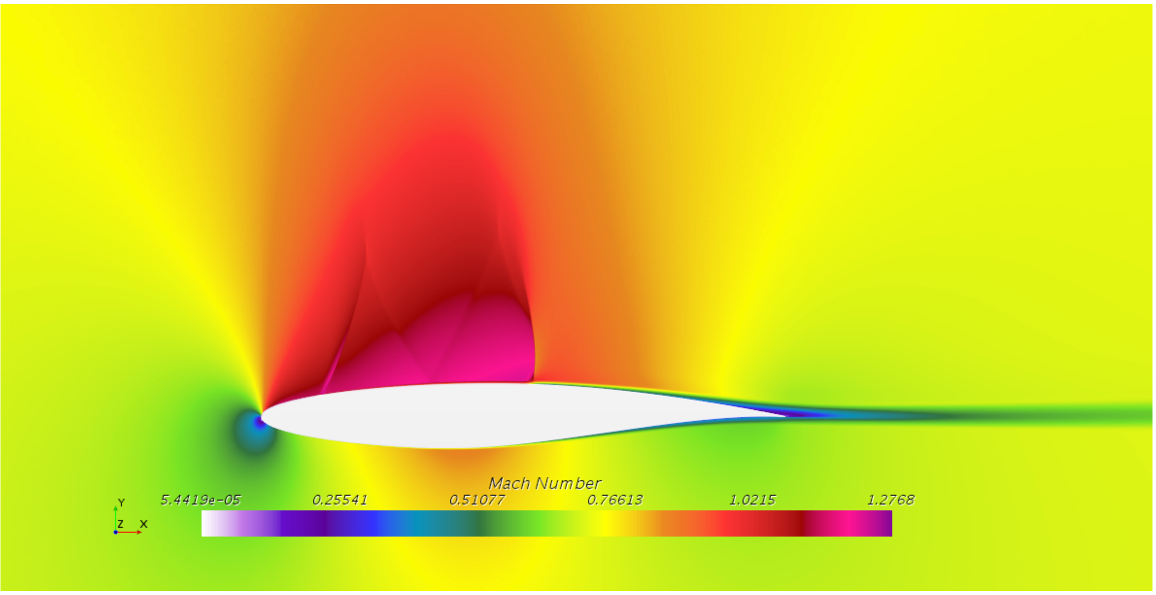

Figure 36: Distribution of the local Mach number around the RAE 2822 airfoil.

The results of the RAE 2822 simulation show that overall the flow can be simulated accurately. However, there are some differences in the locations of the supersonic features as well as some mesh issues at the trailing edge. These differences in the location of the features can be seen in Fig. 35. The downstream shock does not have the exact same cord location as seen in the experiments (0.5 for CFD and 0.55 for experiment) and the initial fan at the leading edge has a slightly lower C_p value for CFD. The location of the shock is highly dependent on the particular experimental flow conditions as well as the solver that was used in the simulation [22] [31] [32]. The trailing edge issue is due to the limitation of Star-CCM+'s mesher not allowing for a finer mesh at the trailing edge tip. However, even with these issues, the flow physics match very well. Specifically, the bottom of the airfoil (that has no step) matches almost exactly, with the only deviation from the experimental data coming at the leading edge fan and the downstream shock. A mesh dependence test was run to further ensure the solution obtained was not dependent on the mesh size. Table 9 shows 3 mesh iterations and their corresponding values of C_n and C_d. As the coefficients clearly follow experimental data and the mesh independence of the solution, the RAE 2822 airfoil was judged to adequately match the experimental data and successfully model the flow over a small step.

Table 9: Mesh dependence of C_n and C_d for the RAE 2822 airfoil simulations.

Mesh	C_n	C_d
400,000	0.733	0.0127
1,200,000	0.735	0.0128
5,000,000	0.736	0.0128
Experimental	0.743	0.0127

5.2.4. 2D Ramp

Following the full scale 2D airfoil simulations, a smaller domain was made to more precisely simulate the flow over the step on the wing. These simulations were performed to see how the addition of a ramp downstream of a BFS would mitigate the negative impacts of the BFS. Fig. 37 shows a local Mach contour plot of the flow over the BFS. The focus of this comparison was to see if the addition of a ramp alters the supersonic features (see Fig. 38).

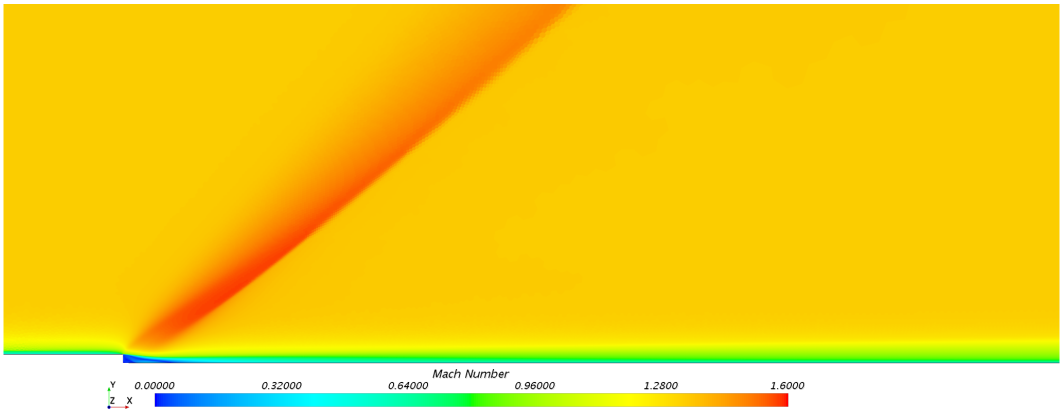

Figure 37: Mach number contour plot showing the flow over a BFS.

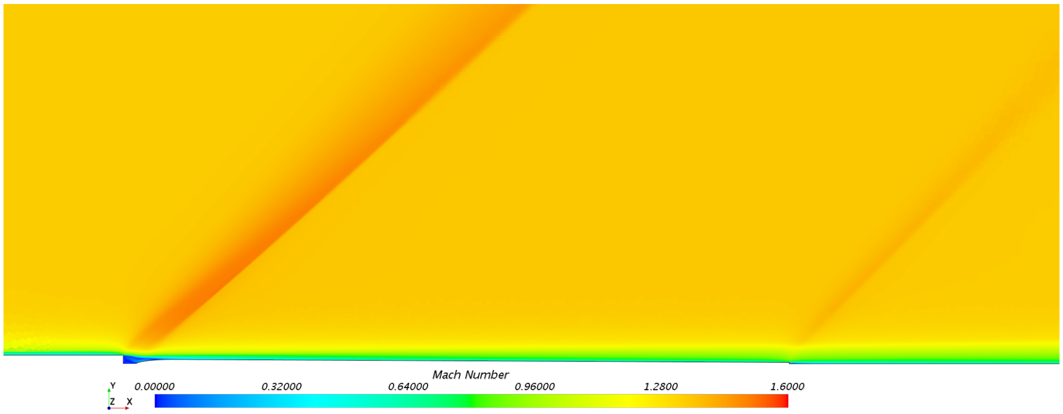

Figure 38: Mach number contour plot showing the flow over a BFS with a downstream ramp.

First, focusing on just the BFS, there is a clear expansion fan forming over the step. This fan causes the flow to increase in speed and results in an increase in pressure drag. Based on insights from Kibble [21], it is determined that the stronger the expansion fan, the larger the increase in pressure drag. Therefore, the metrics of reducing the impact of the BFS on the flow chosen to be investigated were the maximum value of Mach number and the change in total pressure. Next, Fig. 38 shows the same BFS as Fig. 37, but with the addition of a downstream ramp geometry. This Mach contour shows that the addition of the ramp reduced the strength (or maximum Mach value) of the expansion fan over the step. However, this ramp generates an additional, but very weak, fan at the trailing edge of the ramp. Further analysis was then performed by comparing how changing the ramp geometry affected this expansion fan mitigation. Parameters such as upstream ramp height (H_{ru}), downstream ramp height (H_{rd}), ramp length (L_r), and distance of ramp from the BFS (D_r) were altered. Table 10 shows all simulations that were run, along with their corresponding maximum Mach number and total pressure change. This table shows that, based on the geometries tested, the BFS was the worst case, while the best case was a ramp that has an H_{ru} close to the height of the BFS and a minimal D_r. It was also shown that H_{rd} has minimal impact on the effect of the ramp, as long as it remained reasonably small

(< 0.5 mm). This points to the ideal case being an infinite (L_r) ramp, of same (H_{ru}) as the BFS, with zero (D_r) (the equivalent of no BFS), and a minimal downstream step (H_{rd}). Therefore, while conclusions can still be drawn from these results, it is important that the physical constraints be set to limit the range of parameters to what could be deployed on an actual aircraft wing. These restriction are based on the suggested guidelines by the Federal Aviation Administration (FAA) and can be seen in Fig. 39. These guidelines are a minimum BFS (or slat step) height of 2 mm, maximum forward facing step (FFS) height of 0.5 mm, maximum H_{ru} of 1.5 mm, with a minimum slope of 1/5 on the growth from the wall to max H_{ru}.

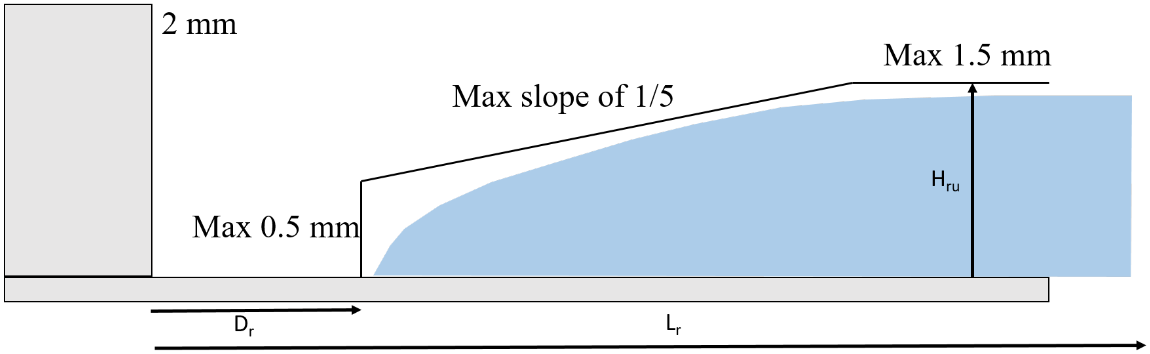

Figure 39: Schematic showing the constraints of the downstream ramp.

Table 10: Changes in ramp parameters versus maximum Mach number and pressure change.

Geometry	Total Pressure Change (Pa)	Max Mach
BFS	90.63	1.585
Prelim Ramp	75.89	1.499
Ramp w/ H_{rd} increased	77.54	1.499
Ramp w/ H_{rd} decreased	75.47	1.499
Ramp w/ L_r increased	75.7	1.498
Ramp w/ H_{ru} increased	70.54	1.429
Ramp w/ D_r increased	76.22	1.466

5.3. Conclusion

Simulations were built to analyze the local flow physics of the CVG in its real world application on a Boeing 737 wing and to analyze the effect of steps and ramps on airfoils. The first sets of simulations were compared to those seen in Chapter IV to see if the effects on wall shear and skin friction were consistent. Next, Q-criterion was utilized to observe the vortex formation of the CVG to see if it, as its name implies, generates significant vortex features. The RAE 2822 simulations were then performed as a necessary step to give credibility to smaller scale models. Following the validation of the RAE 2822 simulations, analyses were performed on a ramp downstream of an aft facing step to see if it was possible to mitigate the negative impact of the step. Four primary conclusions can be made from these investigations:

1. The flight scale CVGs impart a spanwise variation in the wall shear stress of the flow but differs from the laminar scaling.
2. A L/W ratio dependence is seen in both the spanwise variations as well as the averaged values of wall shear.

3. The CVG was shown to produce coherent structures that persisted downstream of the step, specifically, strong vortex formation off the peak and not the valley. A clear difference between the vortex formation off of the CVG versus a traditional BFS was also shown.

4. A ramp downstream of an aft facing step on a airfoil dampens the effects of the expansion fan that is formed on the BFS. It was discovered that altering the ramp geometry can change the effectiveness of the ramp and that the optimal ramp is as close to the height and downstream location of the BFS as allowed by physical constraints.

CHAPTER VI

Conclusions and Recommendations

6.1. Piper Cherokee Validation

Simulations were built to match the conditions of water tunnel testing of a flat plate (with and without a CVG) performed at Oklahoma State University [25]. These simulations had a domain size of 1 m long by 0.3 m wide. Both the flat plate and flat plate with CVG simulations had the same domain size, with the latter containing the CVG step geometry of length 105 mm, width 76 mm, and height 1.5 mm. Computational data was extracted at the location corresponding to the experimental testing for validation purposes. Following validation, computational data was then used to investigate the flow properties as well as compare with further experimental testing performed on the Piper Cherokee aircraft by Edge Aerodynamix. Four primary conclusions can be made from these simulations and comparisons:

1. The flat plate simulation was validated as the boundary layer profile matched experimental data, which followed closely to the Blasius laminar solution.
2. The CVG simulations were verified and validated by comparing boundary layer characteristics with the experimental results as well as analyzing the wall shear stress distribution compared with flight scale observation.

3. The CVG imparts spanwise variation in the wall shear stress of the flow.

4. The wall shear diamonds were found to be a repeatable feature in both CFD and flight testing. These features have both a L/W and Re_H dependence.

6.2. Flight Scale

Simulations were created to investigate the flow physics of the CVG utilizing the local flow physics at the application location on a Boeing 737 wing. These simulations were compared to those seen in Chapter IV to analyze if the conclusions drawn from those simulations were repeated in the different flow regimes of the two simulations. First, wall shear and skin friction were investigated to see if the patterns seen were consistent. Next, Q-criterion was utilized to observe if the CVG, as its name implies, generates significant vortex features. Following these investigations, a 2D RAE 2822 simulation was built for validation and as a necessary step to give credibility to smaller scale models. Lastly, simulations were built looking at the local effects of an aft facing step with a downstream ramp. These simulations were designed to explore if this downstream ramp could negate the negative impact of the step. Four primary conclusions can be made from this investigation:

1. The flight scale CVGs impart a spanwise variation in the wall shear stress of the flow but differs from the laminar scaling.

2. A L/W ratio dependence is seen in both the spanwise variations as well as the averaged values of wall shear.

3. The CVG was shown to produce coherent structures that persisted downstream of the step, specifically, strong vortex formation off the peak and not the valley. A clear difference between the vortex formation off of the CVG versus a traditional BFS was also shown.

4. A ramp downstream of an aft facing step on a airfoil dampens the effects of the

expansion fan that is formed on the BFS. It was discovered that altering the ramp geometry can change the effectiveness of the ramp and that the optimal ramp is as close to the height and downstream location of the BFS as allowed by physical constraints.

6.3. Recommendations

Although a few conclusions have been made on the flow characteristics of CVGs, further work is still necessary. Moving forward, the impact of the following may be evaluated:

1. A more in-depth analysis of the validated simulations and experimental data.
2. Study the impact of different CVG geometries on the flat plate.
3. Acquire validation data for the CVG at actual flight conditions on the Boeing 737 to compare to the results found in this study.
4. Perform simulations to investigate conclusions drawn from [25].
5. Preform further investigation of ramp geometries for utilization downstream of an aft facing step on an airfoil.

REFERENCES

[1] Lin, J. C., “Review of research on low-profile vortex generators to control boundary-layer separation,” *Progress in Aerospace Sciences*, Vol. 38, No. 4-5, 2002, pp. 389–420.

[2] Martínez-Filgueira, P., Fernandez-Gamiz, U., Zulueta, E., Errasti, I., and Fernandez-Gauna, B., “Parametric study of low-profile vortex generators,” *International Journal of Hydrogen Energy*, Vol. 42, No. 28, 2017, pp. 17700–17712.

[3] Aerodynamix, E., “Safiar plans to modify entire fleet,” *https://edge.aero*, 2017, accessed July 1, 2019.

[4] Holden, H., and Babinsky, H., “Vortex generators near shock/boundary layer interactions,” *42nd AIAA Aerospace Sciences Meeting and Exhibit*, 2004, p. 1242.

[5] Katz, J., “Aerodynamics of race cars,” *Annu. Rev. Fluid Mech.*, Vol. 38, 2006, pp. 27–63.

[6] Zhen, T. K., Zubair, M., and Ahmad, K. A., “Experimental and numerical investigation of the effects of passive vortex generators on Aludra UAV performance,” *Chinese Journal of Aeronautics*, Vol. 24, No. 5, 2011, pp. 577–583.

[7] McCormick, D., “Shock-boundary layer interaction control with low-profile vortex generators and passive cavity,” *30th Aerospace Sciences Meeting and Exhibit*, 1992, p. 64.

[8] López Calle, O., “Preliminary study of the effects of vortex generators in ultralight aircraft,” B.S. thesis, Universitat Politècnica de Catalunya, 2015.

[9] Dubey, A., Chheniya, S., and Jadhav, A., "Effect of Vortex generators on Aerodynamics of a Car: CFD Analysis," *International Journal of Innovations in Engineering and Technology (IJIET)*, Vol. 2, No. 1, 2013.

[10] Aider, J.-L., Beaudoin, J.-F., and Wesfreid, J. E., "Drag and lift reduction of a 3D bluff-body using active vortex generators," *Experiments in Fluids*, Vol. 48, No. 5, 2010, pp. 771–789.

[11] Abbott, B., "Boeing 737-800 American Airlines, clean and shiny wing + winglet," *https://www.flickr.com/photos/wbaiv*, 2010, accessed July 1, 2019.

[12] Aerodynamix, E., "Conformal Vortex Generators," *https://edgeaerodynamix.wordpress.com*, 2017, accessed July 1, 2019.

[13] Calvert, M., and Wong, T.-C., "Aerodynamic Impacts of Helicopter Blade Erosion Coatings," *30th AIAA Applied Aerodynamics Conference*, 2012, p. 2914.

[14] Scholbrock, A., "Power performance results using wind turbine blade enhancing devices developed by Edge Aerodynamix," *NREL Technical Report*, 2014.

[15] Kundu, P. K., *Fluid Mechanics*, sixth edition.. ed., Academic Press, 2016.

[16] Fransson, J. H., Shahinfar, S., Sattarzadeh, S. S., and Talamelli, A., "Transition to Turbulence Delay Using Miniature Vortex Generators–AFRODITE–," *Progress in Turbulence V*, Springer, 2014, pp. 71–74.

[17] Von Kármán, T., "Mechanical similitude and turbulence," *National Advisory Committee on Aeronautics*, 1931.

[18] Ferziger, J. H., and Peric, M., *Computational methods for fluid dynamics*, Springer Science & Business Media, 2012.

[19] Spalart, P. R., “Comments on the feasibility of LES for wings, and on a hybrid RANS/LES approach,” *Proceedings of first AFOSR international conference on DNS/LES*, Greyden Press, 1997.

[20] Obara, C., “Boundary layer flow visualization for flight testing,” Tech. Rep. N88-23742, National Aeronautics and Space Administration, May 1986.

[21] Kibble, G. A., “Experimental and Computational Investigation of the Conformal Vortex Generator,” Master’s thesis, Oklahoma State University, Stillwater, 2017.

[22] Kibble, G. A., Jacob, J. D., Alexander, A., Elbing, B. R., Ireland, P., and Black, B., “Aerodynamic Investigation of the Conformal Vortex Generator,” *47th AIAA Fluid Dynamics Conference*, 2017, p. 3117.

[23] Lucido, N., KC, R., Wilson, T., Jacob, J., Alexander, A., Elbing, B., Ireland, P., and Black, J., “Laminar Boundary Layer Scaling Over a Conformal Vortex Generator,” *2019 AIAA Aerospace Sciences Meeting*, 2019.

[24] Lucido, N. A., “Investigation of Low-Profile Vortex Generators on Low Reynolds Number Propellers for Small Unmanned Aircraft,” Master’s thesis, Oklahoma State University, Stillwater, 2019.

[25] KC, R., “Investigation of Low-Profile Vortex Generators via Wake Survey,” Master’s thesis, Oklahoma State University, Stillwater, 2019.

[26] Denaro, F. M., “What does Finite Volume-based implicit filtering really resolve in Large-Eddy Simulations?” *Journal of Computational Physics*, Vol. 230, No. 10, 2011, pp. 3849–3883.

[27] White, F. M., and Corfield, I., *Viscous fluid flow*, Vol. 3, McGraw-Hill New York, 2006.

[28] Haller, G., “An objective definition of a vortex,” *Journal of Fluid Mechanics*, Vol. 525, 2005.

[29] Cook, P., Firmin, M., and McDonald, M., *Aerofoil RAE 2822: pressure distributions, and boundary layer and wake measurements*, RAE, 1977.

[30] Matsuura, K., “DNS Investigation into the effect of Free-Stream Turbulence on Hairpin-Vortex Evolution,” *WIT Transactions on Engineering Sciences*, Vol. 120, 2018, pp. 149–159.

[31] Sadikin, A., Yunus, N. A. M., Hamid, S. A. A., Salleh, S. M., Rahman, M. N. A., Mahzan, S., Ayop, S. S., et al., “A comparative study of turbulence models on aerodynamics characteristics of a NACA0012 airfoil,” *International Journal of Integrated Engineering*, Vol. 10, No. 1, 2018.

[32] Nelson, C., “RAE 2822 Transonic Airfoil: Study 5,” *NASA.gov*, 2008.

VITA

Trevor Wilson

Candidate for the Degree of

Master of Science

Thesis: INVESTIGATION OF LOW-PROFILE VORTEX GENERATORS VIA COMPUTATIONAL METHODS

Major Field: Mechanical and Aerospace Engineering

Biographical:

Education:

Completed the requirements for the Master of Science in Mechanical and Aerospace Engineering at Oklahoma State University, Stillwater, Oklahoma in July, 2019.

Completed the requirements for the Bachelor of Science in Mechanical Engineering at Oklahoma State University, Stillwater, Oklahoma in 2017.